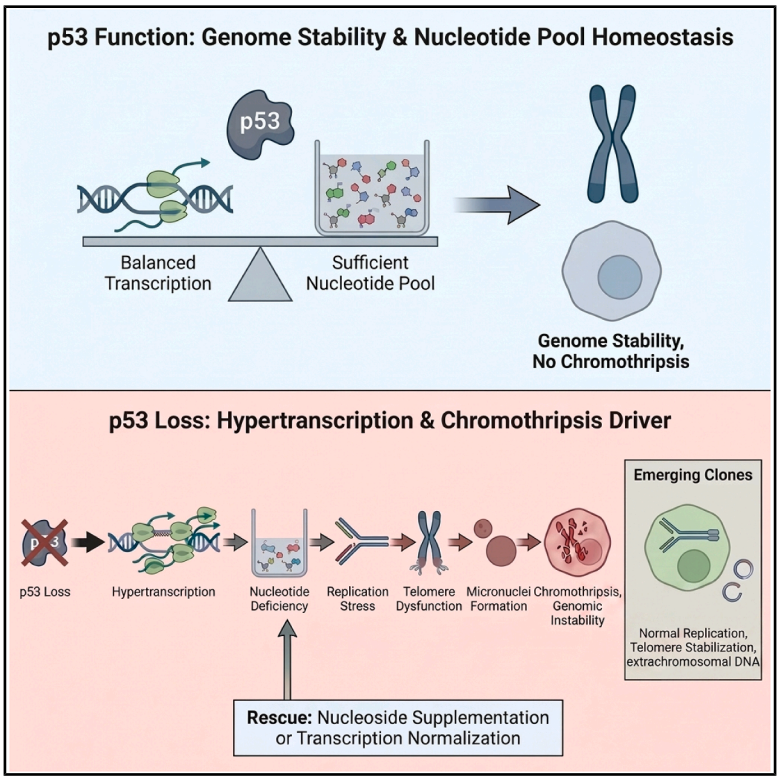
Molecular Cell

Article

Hypertranscription caused by p53 deficiency triggers nucleotide insufficiency that induces replication stress and genomic instability

Graphical abstract



Authors

Wisam Zaatra, George Philippos, Petr Smirnov, ..., Ori Shalev, Batsheva Kerem, Aurélie Ernst

Correspondence

batshevak@savion.huji.ac.il (B.K.), a.ernst@dkfz-heidelberg.de (A.E.)

In brief

Zaatra, Philippos, et al. demonstrate that loss of the tumor suppressor p53 causes excessive transcription that depletes nucleotide pools required for DNA replication. The nucleotide shortage induces replication stress, genomic instability, and chromothripsis. These findings uncover a mechanism by which p53 safeguards genome integrity by restraining transcription and preserving nucleotide homeostasis.

Highlights

- p53 loss induces hypertranscription and excessive nucleotide consumption
- Nucleotide insufficiency causes replication stress and genomic instability
- Replication stress drives telomere dysfunction, micronuclei, and chromothripsis
- Normalization of nucleoside balance or transcription rescues genome instability

Zaatra et al., 2026, Molecular Cell *86*, 3411–3430
September 3, 2026 © 2026 The Authors. Published by Elsevier Inc.
https://doi.org/10.1016/j.molcel.2026.08.003

CellPress

Molecular Cell

CellPress
OPEN ACCESS

Article

Hypertranscription caused by p53 deficiency triggers nucleotide insufficiency that induces replication stress and genomic instability

Wisam Zaatra,[1,14] George Philippos,[2,3,14] Petr Smirnov,[2,4] Shira Milo,[1] Jan Otoničar,[2,3] Michelle Chan,[2] Michal Harel,[5,6,15] Frauke Devens,[2] Tchelet Goldberg,[1] Alexandra Eliassaf,[7] Karen Grimes,[4] Michal Irony-Tur Sinai,[1] Gianluca Sigismondo,[8,9] Kathrin Laue,[10] Uri Ben-David,[10] Tamar Geiger,[5,11,16] Jan O. Korbel,[4,12] Jeroen Krijgsveld,[8,9] Ori Shalev,[7] Batsheva Kerem,[1,17,*] and Aurélie Ernst[2,13,*]

[1]Department of Genetics, The Life Sciences Institute, The Hebrew University, Jerusalem, Israel
[2]Division of Genome Instability, German Cancer Research Center (DKFZ), Heidelberg, Germany
[3]Faculty of Biosciences, University of Heidelberg, Heidelberg, Germany
[4]European Molecular Biology Laboratory, Genome Biology Unit, Heidelberg, Germany
[5]School of Medicine, Tel Aviv University, Tel Aviv, Israel
[6]OncoHost LTD, Binyamina, Israel
[7]The Metabolic Profiling Unit, The Research Core Facility, The Faculty of Medicine, The Hebrew University of Jerusalem, Israel
[8]Division Proteomics of Stem Cells and Cancer, German Cancer Research Center (DKFZ), Heidelberg, Germany
[9]Medical Faculty, Heidelberg University, Heidelberg, Germany
[10]Department of Human Genetics and Computational Medicine, Gray Faculty of Medical & Health Sciences, Tel Aviv University, Tel Aviv, Israel
[11]Weizmann Institute of Science, Rehovot, Israel
[12]Bridging Research Division on Mechanisms of Genomic Variation and Data Science, German Cancer Research Center (DKFZ), Heidelberg, Germany
[13]German Consortium for Translational Cancer Research (DKTK), Heidelberg, Germany
[14]These authors contributed equally
[15]Present address: OncoHost LTD, Binyamina, Israel
[16]Present address: Weizmann Institute of Science, Rehovot, Israel
[17]Lead contact
*Correspondence: batshevak@savion.huji.ac.il (B.K.), a.ernst@dkfz-heidelberg.de (A.E.)
https://doi.org/10.1016/j.molcel.2026.08.003

SUMMARY

p53 plays a central role in the DNA damage response, inducing repair, cell-cycle arrest or apoptosis. Its loss is associated with replication stress and genomic instability. While several underlying mechanisms were suggested, the primary triggers of catastrophic genomic events like chromothripsis, a known driver of tumorigenesis linked with p53 loss, are still unclear. Using p53-depleted epithelial cells and fibroblasts, as well as patient-derived fibroblasts with germline p53 variants that spontaneously undergo chromothripsis, we found that p53 loss causes hypertranscription and increased nucleotide consumption. The resulting nucleotide shortage induces replication stress, causing telomere dysfunction, micronuclei formation, and chromothripsis. These effects were rescued by nucleoside supplementation or normalization of transcription levels, demonstrating a causal link between transcriptional activity, nucleotide availability, and genome stability. Emerging chromothriptic clones displayed restored DNA replication, telomere stabilization, and extrachromosomal DNA, suggesting key features that support clonal selection. We identify nucleotide pool homeostasis as a critical p53 function that suppresses replication stress, prevents chromothripsis, and protects against early tumorigenesis.

INTRODUCTION

Genomic instability is a hallmark and a driving force of cancer development. It increases the likelihood of point mutations and genomic rearrangements, such as deletions, amplifications, translocations and insertions. Collectively, the latter generate the majority of cancer drivers.[1] Next-generation sequencing technologies in cancer genomics have enabled the discovery of complex forms of genomic instability like chromothripsis.[2,3] This type of catastrophic event generates massive chromosomal rearrangements[2,3] and frequently plays a causative role in tumor development.[4]

This is an open access article under the CC BY license (http://creativecommons.org/licenses/by/4.0/).

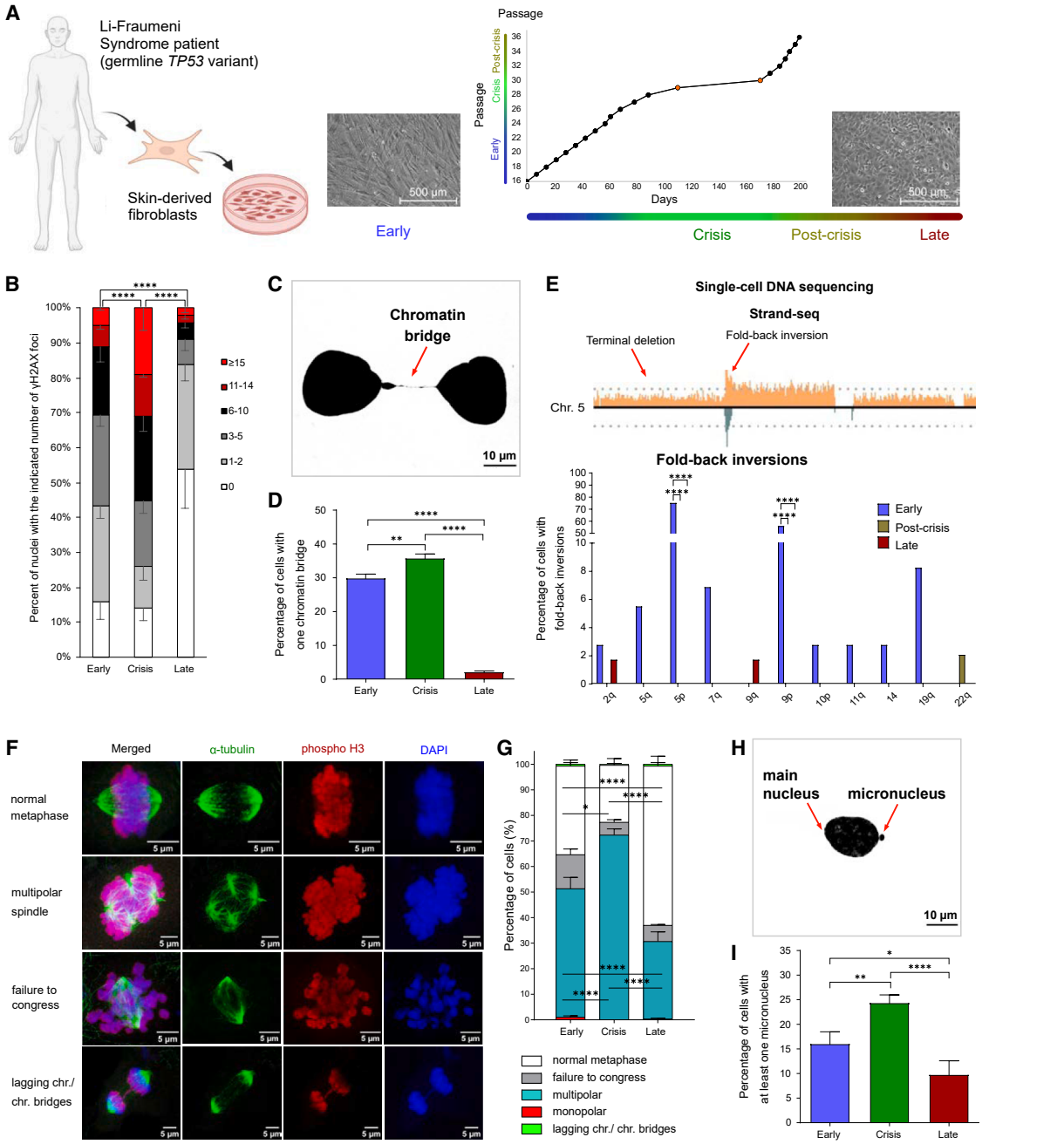


Figure 1. Phenotypic profiling identifies chromatin bridges, multipolar spindles, and micronuclei at early passages

(A) Schematic of the LFS model system showing progression from early passage through crisis to post-crisis stages in patient LFS041. Black circles, splitting ratio 1:3; purple circles, splitting ratio 1:2. Representative images of fibroblast morphology at early and late passages are shown. Scale bar, 500 µm.

(B) Percentage of nuclei with γH2AX foci across passages in LFS041 cells (three independent experiments). Error bars indicate SEM.

(C) Representative chromatin bridge between two cells (DAPI signal). Scale bar, 10 µm.

(D) Quantification of chromatin bridges across passages (750 cells quantified per replicate).

(E) Top, representative fold-back inversion with terminal deletion on chromosome 5, characteristic of BFB cycles detected by strand-seq. Orange and green indicate Watson and Crick strands. Bottom, quantification of fold-back inversions across passages.

(F) Representative immunofluorescence images of normal mitosis and mitotic defects. Scale bar, 5 µm.

(G) Quantification of mitotic defects in early-passage, crisis, and late-passage cells. Data represent mean from three independent experiments. Error bars indicate SEM. "Lagging chr./chr. bridges" indicate lagging chromosomes/chromatin bridges.

(H) Representative micronucleus (DAPI signal). Scale bar, 10 µm.

(legend continued on next page)

Modeling chromothripsis in cell culture has suggested putative underlying mechanisms,[5–8] but whether these play a role in spontaneous chromothripsis events that drive cancer development remains largely unknown. Capturing early stages of cancer evolution in humans is challenging, and it is unclear which sequence of events lead to chromothripsis and how these events confer selective advantages. Our current understanding of what triggers chromothripsis comes either from studying artificially induced chromosome segregation errors in cell lines or indirectly from analyzing genomic data of fully developed tumors, long after chromothripsis has occurred. These studies revealed a strong link between the p53 loss and chromothripsis.[6,9–12] In particular, the prevalence for chromothripsis reaches almost 100% in several tumor types that develop in Li-Fraumeni syndrome (LFS) patients, which carry p53-germline variants.[12,13] Furthermore, for experimental reasons, the studies using externally induced chromothripsis were performed in cells lacking functional p53.[6,7,14] Together, this raises the possibility that the loss of p53 function directly contributes to the induction of chromothripsis.

p53 is one of the most frequently mutated genes in cancer.[15] It is activated by cellular stressors such as DNA damage, oncogene activation, or hypoxia[16–18] and regulates cell-cycle progression, apoptosis, or senescence. Previous studies showed that p53 also regulates DNA replication after DNA damage, either by slowing or accelerating DNA replication rate, depending on cellular systems.[19–22] One study found that p53 loss in a colon cancer model increased transcription-replication conflicts leading to replication stress.[23] However, how p53 regulates and coordinates the interplay between transcription and replication in normal (unstressed) cells, and how its loss contributes to inducing genomic instability, including chromothripsis, remains unclear.

We used longitudinal analyses of primary fibroblasts from LFS patients to investigate the effect of p53 loss and the mechanisms underlying genomic instability including chromothripsis. These cells spontaneously enter a growth crisis, from which a subset of chromothriptic cells escapes and becomes immortalized.[24] During early passages, in cells heterozygous for p53 mutation, we observe mild replication stress, characterized by reduced replication rates, activation of dormant origins, DNA double-strand breaks (DSBs), and micronuclei formation, as well as numerous chromothriptic events, all of which are intensified following p53 loss close to the growth crisis. We also identify clonal selection processes that support cell survival after chromothripsis, including telomere stabilization and amplification of extrachromosomal DNA (ecDNA). Mechanistically, we find that loss of p53 function induces hypertranscription, which enhances nucleotide consumption. The resulting nucleotide deficiency causes replication stress, which drives DNA damage, telomere shortening, micronuclei formation, and chromothripsis. Nucleotide supplementation or normalization of transcription levels rescues replication stress and genomic instability, highlighting the critical role of nucleotide availability in genome maintenance upon p53 loss. Our findings uncover a novel role for p53 in coordinating transcription and nucleotide pools, which is crucial for maintaining genomic stability and preventing early cancer development.

RESULTS

Early-passage LFS cells exhibit DNA damage, which increases during crisis

To investigate the molecular basis of replication stress triggered by p53 loss and its potential link to chromothripsis, we used skin-derived primary fibroblasts from LFS patients (LFS041, LFS087) (Figures 1A and S1A–S1C), heterozygous for wild-type (WT) p53 and with a germline variant in the other allele. To characterize these cells, we mapped the sequence of events leading to chromothripsis by performing longitudinal profiling of genomic instability and phenotypic features associated with chromothripsis, such as DNA DSBs,[6] chromatin bridges,[8,25] mitotic defects,[5,7] and micronuclei[5,6] (i.e., nuclear atypia encapsulating chromosomal fragments or chromosomes). At early passages, we observed a substantial number of DNA DSBs, which markedly increased during crisis and subsequently declined at late passages following immortalization (Figure 1B). Chromatin bridge quantification showed similar kinetics (Figures 1C, 1D, and S1D–S1H). In line with this, strand-specific single-cell DNA sequencing (strand-seq)[26] revealed fold-back inversions followed by terminal deletions characteristic of breakage-fusion-bridge (BFB) cycles in a high fraction of cells (up to 70% on chromosome 5p), evident at early passages (Figure 1E).

In cellular models with externally induced chromothripsis, broken bridge chromosomes undergo frequent mis-segregation during mitosis and form micronuclei.[5] To explore the role of mitotic errors as a source of spontaneous chromothripsis, we quantified mitotic defects in LFS041 and LFS087 fibroblasts and detected high levels at early passages and during crisis, in particular large numbers of multipolar spindles (Figures 1F, 1G, S1E, and S1F). Multipolar spindles cause lagging chromosomes and mis-segregation and are a source of micronuclei.[27] Accordingly, we found high numbers of micronuclei at early-passage LFS cells, with a further increase during crisis (Figures 1H, 1I, and S1G). The fraction of cells with mitotic defects and micronuclei decreased at late passages (Figures 1F–1I). Analyzing control fibroblasts derived from a LFS family member that did not inherit a p53-germline variant (non-LFS, LFS9) showed that these cells, grown in the same conditions, had very low levels of chromatin bridges, micronuclei, and DSBs, significantly lower than in LFS cells (Figures S1H–S1J), indicating that genomic events detected in early-passage LFS cells are distinctive features due to p53 dysfunction. Overall, these data support LFS patient-derived fibroblasts as a model

(I) Quantification of micronuclei across passages. Data represent mean ± SEM from four independent experiments (750 cells quantified per experiment). Statistical significance was assessed using Fisher's exact test with multiple-testing correction in (E), using repeated-measures two-way ANOVA followed by Fisher's LSD test in (G), and using one-way ANOVA followed by Tukey's multiple comparisons test for (D) and (I). *$p < 0.05$, **$p < 0.01$, ***$p < 0.001$, ****$p < 0.0001$. See Figure S1.

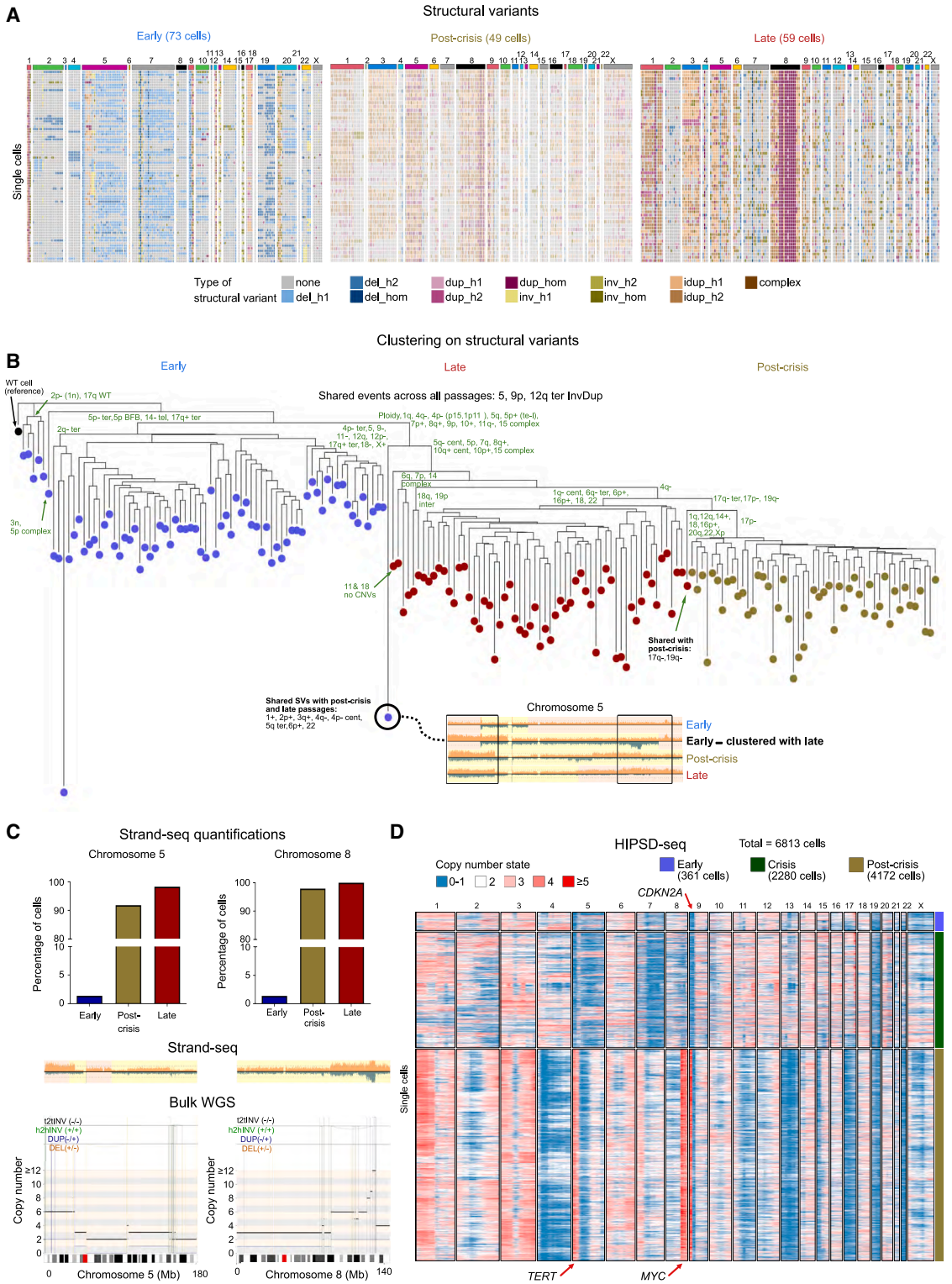


Figure 2. Single-cell DNA sequencing shows a high number and high diversity of chromothriptic events at early passages and later selection of dominant clones

(A) Heatmaps of structural variants per chromosome detected by strand-seq in ≥10% of cells across passages in LFS041. Each row represents a single cell. Deletions (blue), amplifications and complex rearrangements (orange and brown). Del, deletion; dup, duplication; inv, inversion; idup, inverted duplication; h1/h2, homolog 1/2; hom, homologous.

(legend continued on next page)

well suited to study the mechanistic basis of spontaneous chromothripsis.

Dominant clones with chromothripsis appear only after crisis

To characterize dominant chromothriptic clones that emerge, we used strand-seq to determine the timing of chromosomal alterations and to track the longitudinal evolution of these variants. At early passages (p.22), LFS cells exhibited a broad diversity of structural rearrangements, with a majority of deletions (Figures 2A and S2A). In contrast, post-crisis cells (p.63) and late-passage cells (p.343) exhibited more clonal events, suggesting that they passed a selection bottleneck, and more duplications (Figure 2A). The decreasing diversity of genomic structural rearrangements from early to post-crisis and the appearance of dominant clones was supported by lineage-tree reconstruction (Figures 2B and S2B). The distribution of pairwise distances between cells (Figure S2C) and phylogenetic diversity estimates—quantified by adding tree branch lengths per cell group—showed that post-crisis cells (p.63) were genetically closely related to each other, whereas early-passage cells (p.22) showed more diversity (phylogenetic diversity score: 5,072 at p.22 and 2,791 at p.63) (Figure 2B). In late-passage cells (p.349), we observed a renewed increase in diversity, potentially reflecting the accumulation of alterations after long-term culture (phylogenetic diversity score: 5,199 at p.349).

Interestingly, we detected only one early-passage cell that clustered with late-passage cells (Figure 2B). Consistent with this, complex rearrangements detected as clonal in late-passage cells were observed only in minor subpopulations of early-passage cells (Figures 2C and S2D–S2F). This implies that fewer than 5% (Figure 2C) of early-passage cells give rise to the dominant clones observed at later stages, indicating that the vast majority of the complex rearrangements detected at early passages do not have a strong selective advantage. Common events between early and late-passage cells included chromosome 5 alterations, 9p losses, and 12q terminal inverted duplications (Figures 2B, S2B, and S2G).

Chromothripsis has been previously linked with polyploidization,[12–14] but the order by which the events occur vary.[28] In LFS patient-derived fibroblasts, only 1 in 73 early-passage cells was polyploid (ploidy from strand-seq, STAR Methods), while almost one-third (24/73) had at least one complex rearrangement. At late passages (p.63), cells were polyploid (49/49, strand-seq), as confirmed by metaphase spread and whole-genome sequencing (WGS) analysis (Figures S3–S6, S7A, and S7B). Hence, in this model system, complex rearrangements (including chromothripsis) seem to precede genome doubling.

High-throughput single-cell DNA sequencing (HIPSD)[29] on LFS041 (early passage, crisis, and late passage; Figure 2D) and LFS087 cells (late passage; Figure S7C) largely confirmed the strand-seq data, showing high numbers of rearrangements and genetic diversity in early-passage and crisis cells and more clonal events at later passages (Figure 2D). Clonal events detected at early passages that might facilitate chromothripsis (or the survival of chromothriptic cells) included chromosome 9p loss, which contains the *CDKN2A* locus (Figure 2D). *CDKN2A* encodes two tumor suppressors regulating cell cycle and cell death. In post-crisis cells, clonal focal gains that provide a selective advantage and might explain clonal expansion included the oncogene *MYC* (Figure 2D) and telomere reverse transcriptase (*TERT*). Interestingly, at early passages, we detected a *TERT* loss (Figure 2D), suggesting that BFB cycles on chromosome 5p may promote chromothripsis, followed by stabilization via *TERT* gain. Overall, genomic profiling identified known drivers of oncogenesis, which may contribute to clonal selection of LFS cells after crisis.

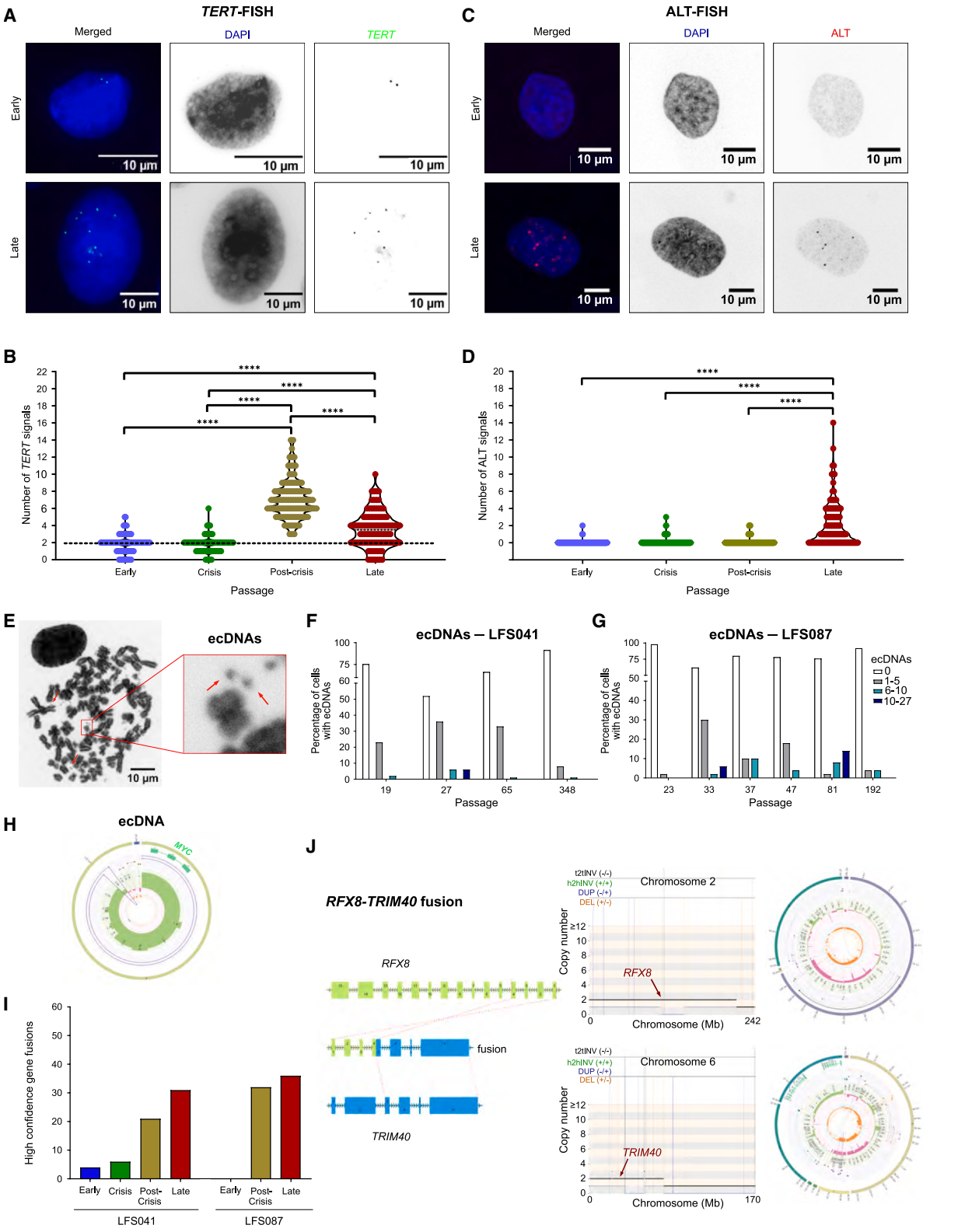
Telomere stabilization, formation of ecDNAs, and gene fusions promote the emergence of dominant clones

Given the high frequency of *TERT* amplification observed in post-crisis cells, we further investigated how dominant clones at late passages avoid senescence and apoptosis, achieve telomere stabilization, and acquire specific drivers. Whereas early-passage LFS041 cells only rarely showed *TERT* gains, we detected cells with high copy numbers of *TERT* after crisis and at late passages, as shown by TERT-fluorescence *in situ* hybridization (TERT-FISH) across passages (Figures 3A and 3B). LFS087 cells acquired telomere stabilization through alternative lengthening of telomeres (ALT) during crisis (Figures 3C and 3D). Clonal telomere stabilization after crisis likely explains the reduction in chromosome bridges in late-passage cells (Figures 1C and 1D) and appears to be a critical driver for dominant chromothriptic clones.

Next, we investigated whether ecDNAs and gene fusions generated by chromothripsis contribute to selective advantages in dominant clones as well. We detected low numbers of ecDNAs at early passages, which increased during crisis and post-crisis (Figures 3E–3G). Assembly from bulk WGS data confirmed the presence of ecDNAs at post-crisis and late passages (Figures 3H and S8A–S8D) that in some cases harbor driver genes (e.g., *MYC*). At late passages, the decrease of ecDNA structures may potentially be explained by their re-integration into linear chromosomes, as reported previously.[30]

Since chromothripsis was shown to generate cancer drivers via gene fusions,[3,31] we investigated gene fusions using bulk

(B) Clustering of single cells based on structural variants using event-based Hamming distance and neighbor joining. Structural variants defining main clusters are indicated at nodes. Shared events are shown in black and cluster-specific differences in green. Bottom, representative chromosome 5 profiles from early-passage, post-crisis, and late-passage cells. "WT-cell" represents an unmodified diploid reference used for phylogenetic rooting. −, loss; +, gain; cent, centromeric; tel, telomeric; term, terminal. The distance between cells reflects the number of events.
(C) Top, frequency of complex rearrangements on chromosomes 5 and 8 across passages. Middle, representative strand-seq examples of rearrangements. Bottom, copy-number profiles from bulk WGS (post-crisis, p.63). t2tINV, tail-to-tail inversion; h2hINV, head-to-head inversion; DUP, duplication; DEL, deletion.
(D) Single-cell copy-number heatmaps (HIPSD-seq; bin size, 1,000 kb) for LFS041 at p.22 (early, $n = 361$), p.27 (crisis, $n = 2,280$), and p.62 (post-crisis, $n = 4,172$). Each row represents a single cell. Post-crisis profiles were corrected for ploidy.
See Figures S2–S7.



(legend on next page)

RNA sequencing (RNA-seq) (STAR Methods). We identified very low numbers of gene fusions (<10 high-confidence fusions/patient) at early passages, as expected due to the absence of clonal chromothriptic events at this stage. Conversely, we detected an increased number of gene fusions from crisis onwards (Figures 3I, 3J, S8E, S9A, and S9B). Exemplarily, chromothripsis led to the formation of a *TRIM40-RFX8* fusion, leading to a 100-fold overexpression of *TRIM40*, normally barely expressed in healthy individuals but described as a pathogenic driver in epithelial cells.[32] Collectively, our data indicate that telomere stabilization, ecDNA, and gene fusion events enable cells to bypass crisis.

Loss of WT p53 function precedes crisis in LFS cells

To investigate the role of p53 in chromothripsis, we examined the p53 status of LFS041 and LFS087 cells at the crisis stage. LFS041 cells carry a germline frameshift mutation in codon 184 of one p53 allele, giving rise to a transcript carrying a premature stop codon, subjected to nonsense-mediated mRNA decay. During crisis, LFS041 cells lose the WT p53 protein, coinciding with emergence of a shorter p53 variant (~50 kDa) (Figure S10A). This variant was identified as the p53 β-isoform, lacking the oligomerization domain[33] (Figure S10B). LFS087 cells also lose the WT allele during crisis (detected by DNA sequencing). This results in the sole expression of the R248W-germline mutant allele (Figure S10C), which leads to loss of WT p53 functions and acquisition of new oncogenic features.[34] To confirm that LFS cells lost WT p53 function during the crisis, we analyzed the expression of two canonical p53-target genes (*p21*, *RRM2B*) following treatment with Nutlin-3a, which activates the p53 pathway. As expected, p53-proficient BJ fibroblasts (control cells) showed a strong increase in *p21* and *RRM2B* mRNA levels upon Nutlin-3a treatment, while crisis LFS041 and LFS087 cells did not (Figure S10D). These results suggest that LFS cells are deficient for WT p53 at the crisis stage (Figure S10E).

Mild replication stress in early-passage LFS cells is enhanced upon p53 loss

p53 loss has been linked to perturbed DNA replication dynamics.[22,23,35] We therefore investigated whether replication stress might be the molecular basis underlying the genomic instability in LFS cells. Using DNA combing[36] to analyze DNA replication dynamics (Figure 4A), we observed that compared to BJ fibroblasts, which harbor two copies of WT p53, early-passage LFS041 cells with only one WT p53 allele already showed slower replication rates (1.1 kilobases per minute [kb/min]), which were further significantly reduced during crisis (0.8 kb/min; Figure 4B). Fork distance showed similar patterns, indicating the firing of additional replication origins (Figure 4B). Late-passage LFS041 cells that escaped from crisis exhibited normalization of replication dynamics (Figure 4B). We also analyzed the replication dynamics and DNA damage in LFS087 cells, for which the earliest available passages for this analysis had lost WT p53. This showed a very slow replication rate and short fork distance as compared to BJ fibroblasts (Figure S10F) together with high DNA damage levels (Figure S10G). These analyses show that even with one WT p53 allele, LFS cells experience mild replication stress, exacerbated upon the complete loss of p53 function. Given that replication stress is a major cause of genomic instability in cancer,[37–39] it might contribute to genomic instability in the context of LFS, including chromothripsis.

p53 loss induces hypertranscription and reduces nucleotide metabolism

To better understand the contribution of loss of WT p53 to replication stress and genomic instability, we performed bulk RNA-seq in early-passage and crisis LFS041 cells. Gene set enrichment and Gene Ontology (GSEA GO) analysis of transcriptomic data identified "DNA replication initiation" (GO:0006270), "DNA-binding transcription activator activity, RNA polymerase II-specific" (GO:0001228), "RNA polymerase I complex" (GO:0005736), and "RNA polymerase III complex" (GO:0005666) as major processes activated upon crisis (Figures 4C, 4D, S10H, and S10I). This raises the possibility that crisis LFS cells experience increased transcription. We detected an increased expression of RNA polymerase I (RNA Pol I) subunits in late passages compared to early passages by RNA-seq in LFS fibroblasts (e.g., *POLR1E*, *POLR1D*, and *POLR1C*; Figure 4D), suggesting a global hypertranscription of ribosomal RNA (rRNA) genes. We therefore analyzed the transcription levels in LFS041 compared to non-LFS primary fibroblasts by quantifying 5-ethynyl uridine (EU) incorporation into nascent RNA. Interestingly, in early-passage LFS041 cells, we detected increased transcription relative to non-LFS cells, which was further increased during the crisis (Figures 4E and 4F).

Figure 3. Telomere stabilization, formation of ecDNAs, and gene fusions promote the emergence of dominant clones

(A) Representative TERT-FISH images in early and late passages. Scale bar, 10 μm.

(B) Quantification of TERT-FISH signals per nucleus in LFS041 cells across passages. Data represent mean ± SEM (100 nuclei per passage). Dashed line indicates diploid TERT copy number (2 copies per cell).

(C) Representative ALT-FISH images in early and late passages. Scale bar, 10 μm.

(D) Quantification of ALT-FISH signals per nucleus in LFS087 across passages. Data represent mean ± SEM from two independent experiments (n = 100 cells per condition).

(E) Representative metaphase showing ecDNA amplification in LFS087 post-crisis cells. Scale bar, 10 μm.

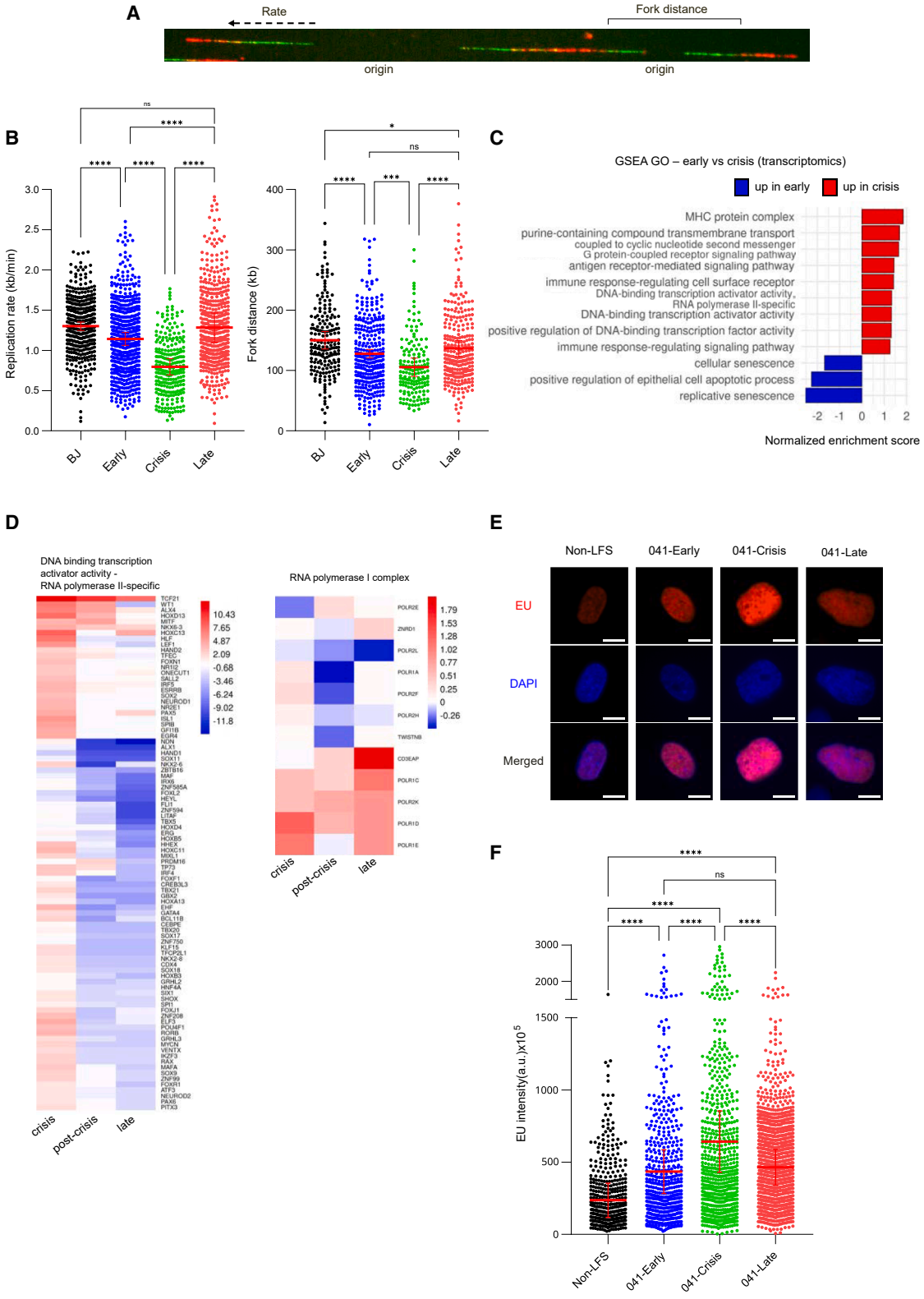
(F and G) Percentage of ecDNA-positive cells in LFS041 (F) and LFS087 (G). n = 50 cells per passage per patient.

(H) ecDNA structure containing *MYC* identified in LFS041 bulk WGS using OncoAnalyser and validated with AmpliconSuite.

(I) Number of high-confidence gene fusions detected by bulk RNA-seq.

(J) Representative *RFX8-TRIM40* gene fusion in LFS087 late-passage cells. Left, breakpoint mapping of *RFX8* (chr2) and *TRIM40* (chr6). Middle, ReConPlot of chromosomes 2 and 6 showing associated structural variants. Right, Circos plot from bulk WGS of LFS087 (p.195) supporting genomic rearrangements. Colors indicate deletions (orange), duplications (blue), head-to-head inversions (green), and tail-to-tail inversions (black). t2tINV, tail-to-tail inversion; h2hINV, head-to-head inversion; DUP, duplication; and DEL, deletion.

For (B) and (D), statistical significance was assessed using Kruskal-Wallis test followed by Dunn's multiple comparisons test. *$p < 0.05$, **$p < 0.01$, ***$p < 0.001$, ****$p < 0.0001$. See Figures S8 and S9.



(legend on next page)

LFS fibroblasts offer a complex model for p53 loss, harboring numerous copy-number alterations, high levels of micronuclei, and telomere shortening. However, the possibility that the mutant p53 in LFS patients may have dominant-negative effects or gain of oncogenic functions cannot be excluded. Thus, to test if the observed transcriptional increase was a direct consequence of p53 loss, we switched to a different model system, namely immortalized BJ-*hTERT* fibroblasts infected with a plasmid expressing a short hairpin against p53 (Shp53). This model allows p53 downregulation without introducing additional perturbations. In these cells, p53 mRNA levels are 20-fold lower relative to control cells expressing a scrambled short hairpin control (Scr), and no p53 protein is detectable (Figures S11A and S11B). We analyzed nascent transcription levels following p53 loss by quantifying EU incorporation into nascent RNA and observed that p53 loss indeed leads to hypertranscription (Figure S11C). This causes a concomitant increase in total cellular RNA levels, as shown by acridine orange staining (Figures S11D–S11F). An association between increased RNA transcription and aneuploidy was recently reported.[40,41] Therefore, we assessed the aneuploidy status of p53-downregulated cells using low-pass WGS, but found no detectable changes (Figure S11G). This suggests that the hypertranscription induced by short-term p53 loss occurs independently of aneuploidy. Altogether, these findings demonstrate that p53 loss is sufficient to induce a global increase in transcriptional activity.

To gain molecular understanding of the consequences of hypertranscription induced by p53 loss, we performed proteomics analyses in BJ cells. Proteomic profiling identified 556 differentially expressed proteins upon p53 downregulation (323 upregulated and 233 downregulated proteins, Welch's t test, $p < 0.05$). Protein-protein-interaction (PPI) network analysis revealed distinct functional clusters among up- and downregulated proteins, including downregulation of the pentose-phosphate pathway (PPP), a critical supplier of ribose-5-phosphate and nicotine adenine dinucleotide phosphate (NADPH) required for nucleotide biosynthesis.[42] Specifically, seven PPP-related proteins (TALDO1, G6PD, PGD, PGM1, GPI, PFKM, and TKT) showed a 3-fold reduction (Figure S12A; Table S1). Among upregulated proteins, PPI analysis revealed clusters involved in replication origin licensing, DNA repair, ribosome biogenesis, nuclear transport, and innate immune response including response to double-stranded RNA—common markers of DNA replication stress and elevated transcriptional activity (Figure S12A). Kyoto Encyclopedia of Genes and Genomes (KEGG) enrichment[43] identified the PPP as the most significantly downregulated biochemical pathway (KEGG:00030, adjusted p value = 5.78×10^{-5}; supplemental information, Figure S12B), consistent with reduced nucleotide metabolism and supporting the PPI results. GO[44,45] and REACTOME[46] enrichment further suggested activation of the Ataxia Telangiectasia and Rad3-related protein -dependent replication stress response (REAC:R-HSA-176187, adjusted p value = 3.95×10^{-3}; Table S2), enhanced DNA repair (GO:0006281, adjusted p value = 2.736×10^{-5}; Table S2), replication initiation (GO:0006270, adjusted p value = 1.1×10^{-3}; Table S2), and reduced nucleotide biosynthesis (GO:0009117, adjusted p value = 0.014; Table S3) following p53 downregulation. Overall, the proteomic analysis in BJ cells indicates that p53 loss leads to increased transcriptional activity and additionally uncovers a reduced nucleotide biosynthesis upon p53 loss.

p53 loss disrupts the nucleotide pool, leading to replication stress, DNA damage, and micronuclei formation

As p53 loss increases transcriptional activity while simultaneously limiting nucleotide biosynthesis, we hypothesized that elevated consumptions of ribonucleotides (the RNA building blocks), together with decreased nucleotide biosynthesis, may result in decreased pools of cellular deoxynucleotides (the DNA building blocks originating from ribonucleotide diphosphates) and contribute to replication stress and DNA damage. Therefore, we investigated the effects of p53 downregulation on the cellular nucleotide pools. To this end, we performed untargeted metabolomic analysis using liquid chromatography-mass spectrometry (LC-MS) in BJ cells following p53 downregulation. Pathway enrichment and impact analyses revealed the PPP, pyrimidine, and purine metabolism pathways among the top downregulated pathways (Figures 5A, S12C, and S12D). The levels of metabolites such as ribose-5-phosphate and all four nucleosides, adenosine, uridine, guanosine, and cytidine (AUGC), were significantly reduced following p53 downregulation (Figure 5B). This confirms previous work documenting decreased nucleotide levels upon p53 loss.[47–50]

Previous studies reported that replication dynamics is largely determined by the size of the nucleotide pool.[51,52] Furthermore, nucleotide insufficiency, induced by RRM2 downregulation or folate depletion in normal fibroblasts, results in replication stress and accumulation of DNA damage.[53,54] Thus, this raises the possibility that nucleotide insufficiency underlies genomic instability induced by p53 loss. To test if a reduced nucleotide pool affects

Figure 4. Loss of p53 in LFS cells induces replication stress and hypertranscription

(A) Representative combed DNA fiber showing two adjacent outgoing replication origins and converging forks toward termination (central red region).

(B) Distribution of replication fork rate (kb/min, left) and fork distance (kb, right) in BJ control and LFS041 cells across passages. Each dot represents a single measurement. Red lines indicate mean ± SEM across three independent experiments. Statistical analysis was performed using one-way ANOVA.

(C) GSEA of Gene Ontology terms comparing early (p.19) and crisis (p.29) LFS041 fibroblasts using bulk RNA-seq.

(D) Differential expression of DNA-binding transcription activator activity (RNA Pol II-specific, left) and RNA Pol I complex genes (right). Heatmaps show differentially expressed genes (DEGs) across early (p.19), post-crisis (p.65), and late (p.346) passages relative to early passage. Colors reflect NOISeq-derived expression changes (red, upregulation; blue, downregulation).

(E) Representative EU-incorporation images (Alexa Fluor 594) in non-LFS control (LFS8, healthy relative of LFS patient, no *TP53*-germline variant) and LFS041 cells across early, crisis, and late passages. Scale bar, 10 μm.

(F) Quantification of nuclear EU intensity in non-LFS and LFS041 cells across passages. Each dot represents one cell. Red lines indicate mean ± SEM from two independent experiments. Statistical analysis was performed using one-way ANOVA. *$p < 0.05$, **$p < 0.01$, ***$p < 0.001$, ****$p < 0.0001$.

See Figure S10.

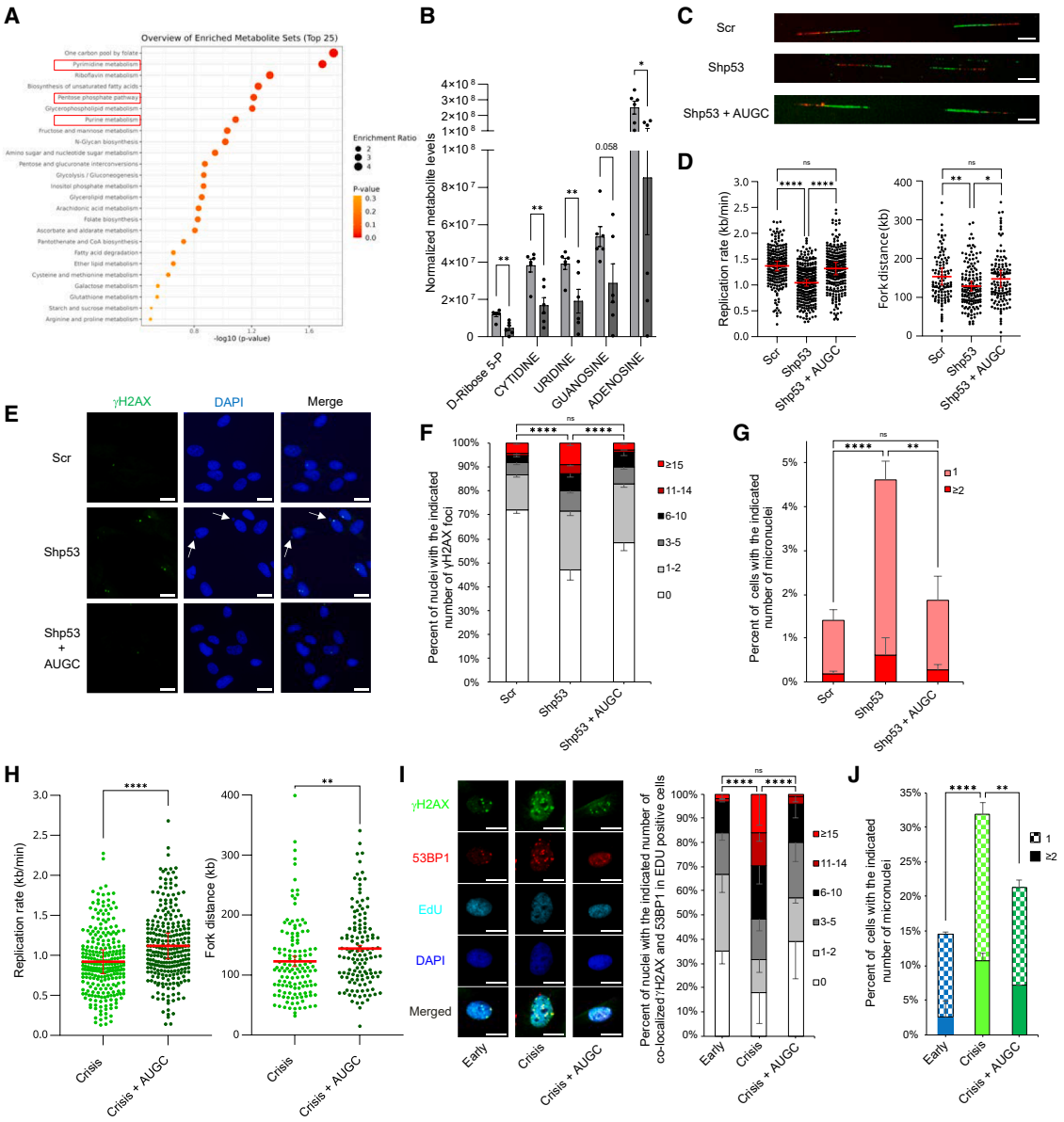


Figure 5. p53 loss by itself decreases the nucleotide pool, leading to replication stress and genomic instability

(A) Pathway enrichment analysis in BJ cells based on LC-MS metabolomics comparing scr and Shp53 cells (six biological replicates/condition). Red boxes highlight nucleotide biosynthesis-related pathways.

(B) LC-MS-based metabolite levels of D-ribose-5-p and nucleosides in scr and Shp53 cells. Lines indicate mean ± SEM from six biological replicates/condition. Statistical analysis was performed using unpaired *t* test.

(C) Representative combed DNA fibers from scr, Shp53, and Shp53 + AUGC (48 h) cells. Scale bar, 10 μm.

(D) Distribution of replication fork rate (kb/min, left) and fork distance (kb, right) in scr, Shp53, and Shp53 + AUGC (48 h) cells. Each dot represents a single measurement. Red lines indicate mean ± SEM across three independent experiments. Statistical analysis was performed using one-way ANOVA.

(E) Representative γH2AX immunofluorescence images in scr, Shp53, and Shp53 + AUGC (48 h) cells. White arrows indicate micronuclei. Scale bar, 20 μm.

(F) Percentage of nuclei with γH2AX foci in scr, Shp53, and Shp53 + AUGC cells. Four independent experiments. Error bars, SEM. Mann-Whitney rank-sum test was used.

(G) Percentage of cells with micronuclei in scr, Shp53, and Shp53 + AUGC cells. Three independent experiments. Error bars, SEM. Chi-squared test was used to compare distributions.

(H) Distribution of replication fork rate (kb/min, left) and fork distance (kb, right) in LFS041 crisis cells and crisis cells supplemented with long-term nucleoside supply. Each dot represents a single measurement. Red lines indicate mean ± SEM across two independent experiments. Unpaired *t* test was used.

(legend continued on next page)

the replication dynamics in BJ cells, we used DNA combing and observed a significant decrease in the mean replication rate and replication fork distance in p53-downregulated cells (Figures 5C and 5D), in agreement with previous studies.[22,23] Interestingly, exogenous supply with the four nucleosides AUGC increased the replication rate and fork distance, indicating a rescue from replication stress (Figures 5C and 5D). We next examined the effect of nucleoside supplementation on replication dynamics and DNA damage in control Scr cells. Supplementation had no detectable effect (Figures S12E and S12F), indicating that this effect is specific to conditions of nucleotide insufficiency, such as those found in p53-downregulated cells. Moreover, p53 downregulation markedly increased DSBs and micronuclei formation, both of which were rescued by nucleoside supplementation (Figures 5E–5G). Collectively, this suggests that p53 loss limits the nucleotide pool available for DNA replication, leading to replication stress and genomic instability.

Nucleotide insufficiency leads to replication stress-induced genomic instability in crisis LFS cells

Metabolomic analysis on early-passage LFS041 cells harboring heterozygous *TP53* revealed a significant reduction in nucleotide metabolites compared to non-LFS fibroblasts (Figure S13A), indicating that nucleotide insufficiency is already present in early-passage cells. Although crisis cells were not analyzed due to cell number limitations, the reduction in nucleotide metabolites likely exacerbates during the crisis after total p53 loss. To test if nucleotide insufficiency plays a role in replication stress and genomic instability in LFS cells during crisis, we supplemented LFS041 with exogenous nucleosides starting at pre-crisis passages (p.22). Nucleoside supply significantly increased the replication rate and fork distance in these cells, indicating a rescue from replication stress (Figures 5H and S13B). Exogenous nucleoside supply also reduced DNA damage levels (Figures 5I and S13C). To investigate whether nucleotide insufficiency contributes to genomic instability, including chromothripsis, we quantified micronuclei formation under nucleoside supply. Nucleoside supply significantly reduced micronuclei formation (by 34%, p value = 1.1×10^{-4}) in crisis LFS041 cells (Figure 5J). Nucleoside supplementation significantly increased replication rate and reduced DNA damage and micronuclei formation in crisis passages from additional LFS patients (Figure S13D–S13F). Together, this indicates that an insufficient nucleotide pool is the molecular basis for the replication stress and genomic instability in crisis LFS cells. Although late-passage LFS cells lost the WT p53 protein (Figure S13G), they rescued their replication stress-induced genomic instability (Figures 1B and 4B). One suggested possibility is that this occurs through *MYC* amplification (Figure 2D), which would lead to the observed upregulation of *MYC*-target genes involved in *de novo* nucleotide biosynthesis (Figure S13H), as we previously found in oncogene-expressing cells.[55]

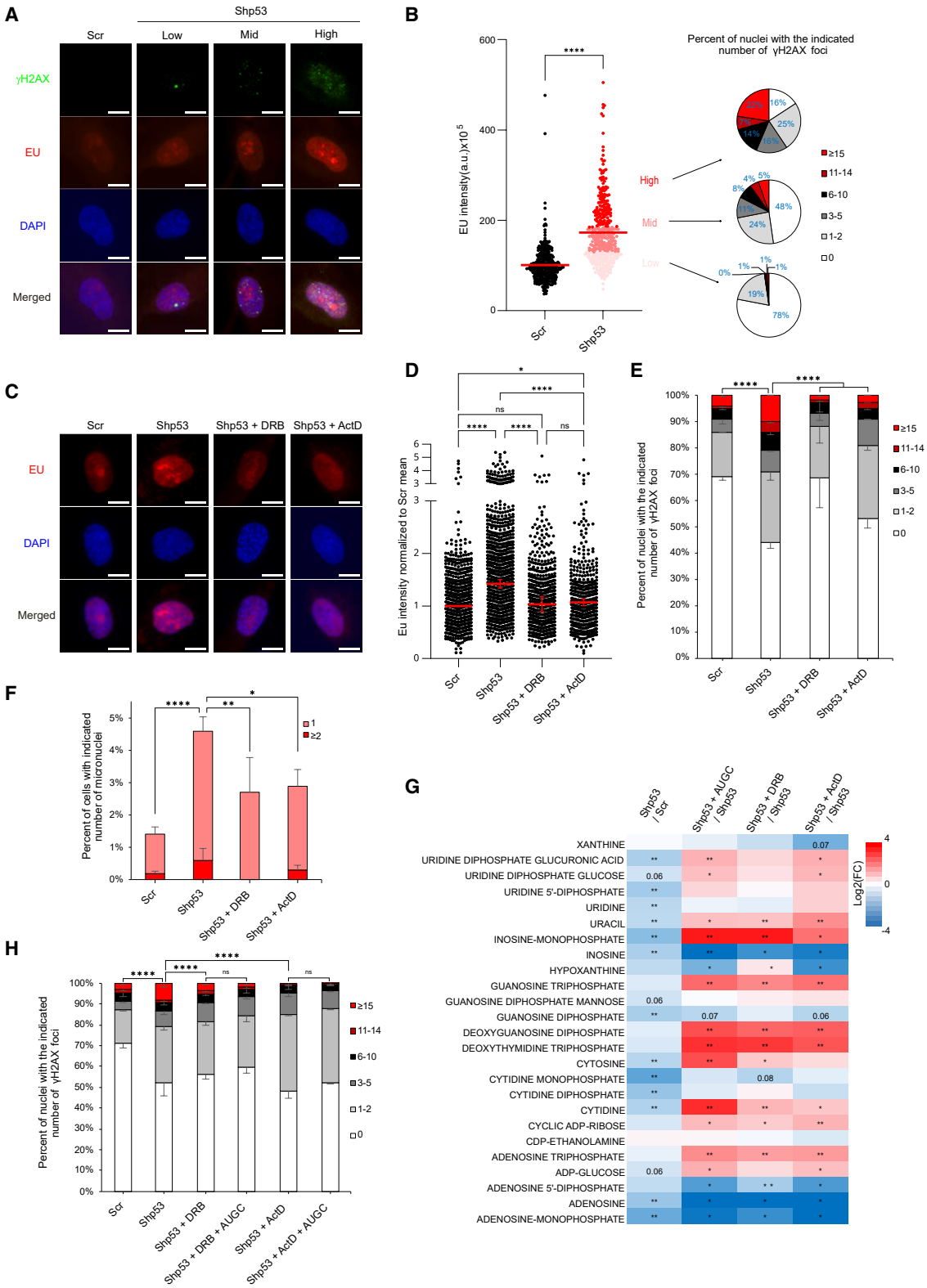
An insufficient nucleotide pool leads to a growth crisis in LFS cells

Exogenous nucleoside supply also increased cell proliferation, as indicated by the percentage of 5-ethynyl-2'-deoxyuridine (EdU)-positive cells in crisis LFS cells (Figure S13I). LFS041 cells entered crisis after six population doublings, at p.29 (Figures S13J–S13L), whereas LFS041 cells supplemented with nucleosides continued to proliferate for nearly four additional population doublings before eventually stopping proliferation, at p.35 (Figures S13J–S13L). To further investigate the possibility that nucleoside supply might prevent further telomere shortening caused by replication stress, which might be the cause of the growth crisis, we treated LFS041 cells with a long-term exogenous nucleoside supply (starting from early passage) and quantified telomere length using the Telosizer assay.[56] Interestingly, nucleoside supply prevented telomere shortening and crisis (Figure S13M). Altogether, we demonstrate that nucleoside supply rescues the replication stress, leading to rescue of DNA damage, micronuclei formation, and telomere shortening and preventing the premature cellular proliferation crisis. Our findings further indicate that nucleotide insufficiency in p53-loss cells plays a major role in promoting genomic instability, resulting in a growth crisis from which chromothriptic cells emerge.

Hypertranscription causes excessive nucleotide consumption, leading to genomic instability

To determine if hypertranscription contributes to elevated levels of DNA damage induced by p53 downregulation, we quantified EU incorporation into nascent RNA following p53 downregulation in BJ cells by dividing the EU intensity into terciles (high, mid, and low). In high-EU nuclei, the level of DNA damage was high, whereas in nuclei showing low EU, the level was very low (Figures 6A and 6B). To test whether hypertranscription is the source of DNA damage following p53 downregulation, we reduced nascent transcription levels to those observed in Scr cells using either the RNA Pol II inhibitor 5,6-dichloro-1-β-D-ribofuranosylbenzimidazole (DRB) or the RNA Pol I inhibitor actinomycin D (ActD) (Figures 6C and 6D). This showed a significant reduction in DNA damage and micronuclei formation in cells treated with either transcription inhibitor (Figures 6E and 6F). LC-MS in p53-downregulated BJ cells treated with DRB or ActD showed a significant increase of 9/25 (36%) and 11/25 (44%) of the analyzed nucleotide metabolites, respectively. Eight of the increased metabolites (uracil, inosine monophosphate, guanosine triphosphate, deoxyguanosine diphosphate, deoxythymidine triphosphate, cytidine, cyclic ADP-ribose, adenosine triphosphate) were shared between both transcription inhibition treatments and following AUGC supply (Figure 6G). To investigate whether transcription normalization eliminates the effect of nucleotide supplementation, we supplemented p53-downregulated cells with nucleosides in the presence of the transcription inhibitors DRB or ActD. Nucleoside supplementation had

(I) Co-localization of γH2AX (green) and 53BP1 (red) foci in LFS041 EdU-positive early cells, crisis cells, and crisis cells supplemented with long-term nucleoside supply. Two independent experiments. Error bars, SEM. Representative images (left) and quantification (right). Scale bar, 20 μm. Mann-Whitney test was used. (J) Percentage of miconuclei in LFS041 early cells, crisis cells, and crisis cells supplemented with AUGC cells. Three independent experiments. Error bars, SEM. Chi-squared test was used to compare distributions. $^{*}p < 0.05$, $^{**}p < 0.01$, $^{***}p < 0.001$, $^{****}p < 0.0001$.
See Figures S11–S13.



(legend on next page)

no additional effect on DNA damage levels in cells treated with transcription inhibitors (Figure 6H). These findings directly show that the hypertranscription is the cause for nucleotide insufficiency, and its normalization is sufficient to restore it. Taken together, our results indicate that hypertranscription driven by p53 loss leads to excessive nucleotide consumption, resulting in replication stress leading to genomic instability.

p53 loss drives hypertranscription in epithelial cells and human cancers

Most human cancers arise from epithelial cells. Thus, to investigate whether the hypertranscription induced by p53 loss observed in fibroblasts (LFS and BJ, Figures 4 and 6) is a general phenomenon and relevant to cancer, we studied the effect of p53 loss in non-transformed MCF10A breast epithelial cells. In these cells, CRISPR-induced p53 knockout resulted in significantly reduced mRNA levels compared with cells infected with a sgLacZ control plasmid (sgCTRL) (Figure S14A). We then analyzed the nascent transcription following p53 knockout by quantifying EU intensity and found that p53 loss indeed induces hypertranscription in epithelial cells (Figure S14B). To determine whether hypertranscription contributes to the elevated DNA damage observed upon p53 knockout, EU signal intensity was divided into terciles (high, mid, and low). As found in fibroblasts, nuclei with high EU incorporation exhibited high levels of DNA damage, whereas nuclei with low EU incorporation showed very low damage (Figure 7A), suggesting that hypertranscription induced by p53 loss underlies the genomic instability observed in these epithelial cells. Exogenous nucleoside supplementation rescued the DNA damage in the MCF10A-sg*TP53* cells (Figure 7B), with no effect in MCF10A sgCTRL cells (Figure S14C). Furthermore, reducing transcriptional activity in MCF10A-sg*TP53* cells using DRB or ActD (Figure 7C) resulted in a significant reduction in DNA damage (Figure 7D) and micronuclei formation (Figure 7E). Altogether, this indicates that hypertranscription induced by p53 loss is the underlying mechanism of genomic instability in MCF10A epithelial cells, supporting its role as a common mechanism across different cell types.

To further investigate the link between p53 dysfunction and hypertranscription in cancer, we compared hypertranscription scores, calculated from RNA-seq analyses, between cancers with and without p53 alterations (Figure 7F).[40] Importantly, p53 inactivation is associated with higher hypertranscription scores both in the pan-cancer context (Figure 7F) and in tumor-entity-specific analyses (Figures S14D–S14K). The effect size observed for p53 inactivation was comparable to hypertranscription associated with *MYC* amplification (Figure S14L), a known hypertranscription driver.[40,57,58] Previous studies showed that *MYC* is transcriptionally repressed in a p53-dependent fashion.[59,60] Importantly, the difference in hypertranscription between p53-proficient and -deficient tumors was significant irrespective of *MYC* status (Figure S14M) and across tumor stages I–III (Figures S14N–S14Q). We further analyzed *MYC* expression levels in BJ, LFS, and MCF10A cells. *MYC* expression did not show any detectable change following p53 loss (Figure S14R). Thus, the hypertranscription following p53 loss is likely not dependent on *MYC* activation. Altogether, this supports the relevance of the identified molecular mechanism of hypertranscription caused by p53 deficiency in human cancer development.

DISCUSSION

Here we performed longitudinal analyses of primary fibroblasts from LFS patients to define the sequence of events leading to chromothripsis and to determine the role of p53 loss. Early LFS cells retaining one WT p53 allele already displayed mild hypertranscription, replication stress, and DNA damage, whereas complete loss of WT p53, before crisis, was associated with exacerbated hypertranscription, replication stress, and genomic instability, including chromothripsis, and dominant clone emergence. Acute p53 depletion in BJ fibroblasts and MCF10A epithelial cells similarly induced hypertranscription, resulting in nucleotide depletion, which induces replication stress, DNA damage, and micronuclei formation. This supports a role for p53 in coordinating transcriptional activity with nucleotide availability to preserve genomic stability. Altogether the results suggest that this mechanism operates across cell types (Figure 7G). Transcription can interfere with DNA replication through collisions between the two machineries.[61] Previous work proposed that p53 prevents such transcription-replication conflicts.[23] Our data reveal an additional mechanism for the effect of transcription on replication, showing that the primary impact is through nucleotide depletion, which promotes replication stress. Because transcription is a major nucleotide

Figure 6. p53 loss by itself induces hypertranscription, resulting in nucleotide consumption and genomic instability in BJ fibroblasts

(A) Representative images of γH2AX (green), EU (red), and nuclei (blue) in scr and Shp53 cells grouped into low-, mid-, and high-EU terciles. Scale bar, 10 μm.

(B) Left, nuclear EU intensity in scr and Shp53 cells. Right, γH2AX foci distribution across Shp53 EU terciles. Data are from one representative experiment of three independent experiments. Each dot represents a single cell. Student's *t* test was used.

(C) Representative γH2AX (green), EU (red), and nuclei (blue) images of scr, Shp53, and Shp53 cells treated with DRB (48 h) or ActD (3 h). Scale bar, 10 μm.

(D) Nuclear EU intensity normalized to scr across conditions. Data represent mean ± SEM from independent experiments (scr, $N = 5$; Shp53, $N = 5$; Shp53 + DRB, $N = 3$; Shp53 + ActD, $N = 2$). One-way ANOVA was used.

(E) Percentage of nuclei with γH2AX foci across conditions. Two independent experiments. Error bars, SEM. Mann-Whitney test was used.

(F) Micronucleus frequency across conditions. Data from independent experiments (scr, $N = 3$; Shp53, $N = 3$; Shp53 + DRB, $N = 2$; Shp53 + ActD, $N = 2$). Chi-squared test was used.

(G) Heatmap of log fold changes in metabolite levels from LC-MS comparing scr, Shp53, and Shp53 + AUGC, DRB, or ActD (six biological replicates per condition). Same Shp53 dataset used across comparisons. Red indicates increased and blue decreased metabolites relative to each condition. *p* values were calculated using one-sided *t* tests.

(H) Percentage of nuclei with γH2AX foci in scr, Shp53, and Shp53 treated with transcription inhibitors with or without AUGC supplementation as indicated. Two independent experiments. Error bars, SEM. Mann-Whitney test was used. $^{*}p < 0.05$, $^{**}p < 0.01$, $^{***}p < 0.001$, $^{****}p < 0.0001$.

See Figures S11–S13.

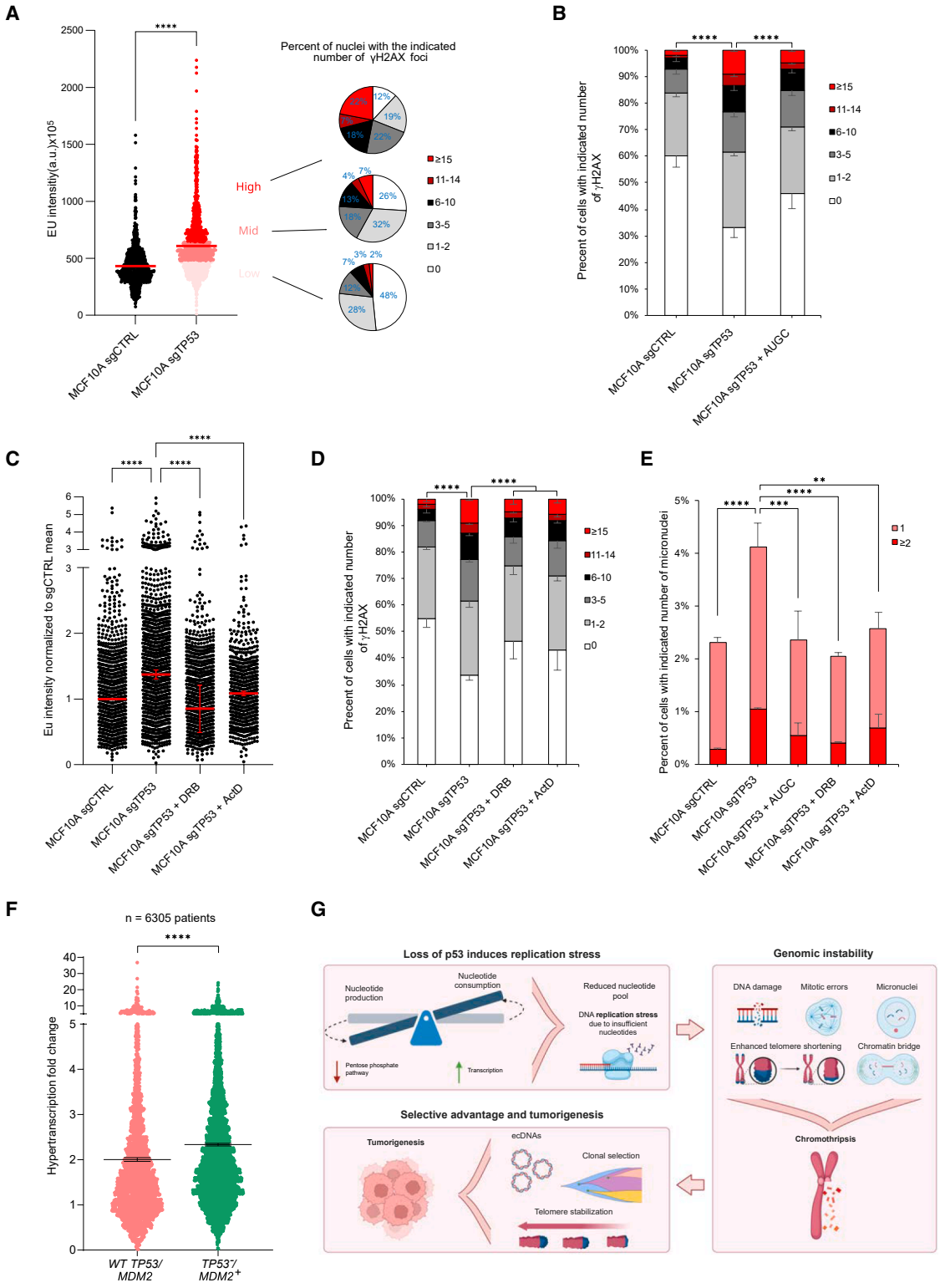


Figure 7. p53 loss by itself drives hypertranscription-induced genomic instability in MCF10A epithelial cells

(A) Left, nuclear EU intensity in MCF10A sgCTRL and sg*TP53* cells. Right, γH2AX foci distribution across sgTP53 EU terciles. Data are from one representative experiment of two independent experiments. Each dot represents a single cell. Student's *t* test was used.

(B) Percentage of nuclei with γH2AX foci in MCF10A sgCTRL, sg*TP53*, and sg*TP53* + AUGC. Two independent experiments. Mann-Whitney test was used.

(legend continued on next page)

consumer,[62] increased transcription reduces nucleotide availability for DNA synthesis. Accordingly, exogenous AUGC supplementation rescued replication stress caused by p53 loss. Inhibition of mRNA or rRNA transcription also reduced genomic instability, indicating that transcription itself is the underlying driver. Nucleoside supplementation had little effect in control cells (Figures S12E, S12F, and S14V), suggesting that rescue occurs specifically under replication stress conditions. Together, these findings demonstrate that hypertranscription directly causes nucleotide insufficiency and that restoring nucleotide balance alleviates replication stress. Our results may also explain the increased transcription-replication conflicts reported previously.[23] Furthermore, a recent work showed that p53 loss derepresses heterochromatin, increasing microsatellite transcription, R-loop formation, and genomic instability,[63] further confirming that WT p53 loss promotes global hypertranscription. Our findings are also consistent with previous studies linking p53 and nucleotide deficiency.[47–50]

Patient-derived LFS fibroblasts spontaneously progress toward immortalization and therefore model early cancer development. LFS is a classic example of p53 haploinsufficiency.[64–66] Early-passage LFS041 fibroblasts carrying a germline frameshift mutation while retaining one WT allele already exhibited replication stress, DNA damage, and genomic instability (Figures 1, 2, and 4). This suggests that p53 heterozygosity perturbs replication and predisposes cells to genomic alterations and eventual loss of heterozygosity. We also found that insufficient nucleotides contribute to crisis by accelerating telomere shortening. Nucleoside supplementation delayed crisis and prevented telomere erosion, consistent with evidence that telomere length is influenced by thymidine metabolism.[67] These findings further support mouse studies showing chromosome fusions and aggressive tumorigenesis following telomere shortening and subsequent telomerase reactivation.[68]

Previous analyses of precancerous non-small cell lung carcinoma identified DNA damage and fragile-site instability as early features of tumorigenesis.[37] Our findings in early-passage LFS cells similarly establish replication stress and DNA damage as early events in cancer development. Under these conditions, cells with advantageous adaptations may be selected. Late-passage LFS041 cells displayed clonal dominance, enhanced proliferation, improved survival, and reduced sensitivity to chronic replication stress. One explanation is increased nucleotide biosynthesis through *MYC* amplification (Figures S13G and S13H), consistent with replication stress driving *MYC* amplification and restoring nucleotide pools.[55] Although this possibility requires further study, our data underscore the role of replication stress in clonal evolution.

Hypertranscription is common in cancer and associated with aggressive disease and poor outcome.[40] Analysis of The Cancer Genome Atlas (TCGA) data confirmed associations between hypertranscription and p53 inactivation in human tumors (Figures 7F and S14D–S14K). Although MYC is a well-established driver of hypertranscription,[40,56,57] our results show that p53 loss induces hypertranscription independently of *MYC* (Figures 4E, 4F, S11C, S14A, S14B, S14L, S14M, and S14R). This supports the relevance of our spontaneous model for identifying molecular events driving crisis and crisis escape. Impaired p53 function facilitated crisis bypass and was associated with recurrent events such as chromosome 15 chromothripsis and telomere stabilization, suggesting positive selection. Chromothripsis generates unstable derivative chromosomes promoting oncogenic alterations, clonal diversification, and intratumor heterogeneity.[69,70] However, only a minority of chromothriptic events produced dominant clones. Single-cell analyses enabled the detection of rare events and detailed reconstruction of clonal evolution, revealing extensive rearrangement diversity before selection of clones carrying advantageous alterations such as *TERT* and *MYC* amplifications, potentially via chromothripsis-generated ecDNA.

We previously showed that aberrant activation of retinoblastoma protein (Rb)-E2F induces replication stress by promoting S-phase entry without sufficient induction of nucleotide biosynthesis, resulting in nucleotide insufficiency.[55] Subsequent studies similarly identified nucleotide depletion as a key driver of oncogene-induced replication stress.[53,71] Our finding that p53 loss disrupts nucleotide availability further emphasizes nucleotide insufficiency as a central mechanism underlying replication stress and genomic instability in cancer. The observation that hypertranscription induces nucleotide depletion, genomic instability, and chromothripsis may provide new opportunities to target nucleotide metabolism in p53-deficient cancers.

Limitations of the study

Although long-term passaging can alter cells, our core findings are based on early passages, and this spontaneous model faithfully recapitulates the *in vivo* chromothriptic process. As in patient tumors,[13,72] loss of WT *TP53* occurs early in patient-derived fibroblasts (Figure S10). Telomere lengthening mechanisms are initially inactive but become active at later passages,[24] evidenced by telomere length, ALT activity, and *TERT* copy-number

(C) Nuclear EU intensity normalized to sgCTRL across conditions. Data represent mean ± SEM from independent experiments (sgCTRL, $N = 3$; sgTP53, $N = 3$; sg*TP53* + DRB, $N = 2$; sg*TP53* + ActD, $N = 2$). One-way ANOVA was used.
(D) Percentage of nuclei with γH2AX foci across conditions. Data represent independent experiments (sgCTRL, $N = 4$; sgTP53, $N = 4$; sg*TP53* + DRB, $N = 3$; sg*TP53* + ActD, $N = 3$). Error bars, SEM. Mann-Whitney test was used.
(E) Micronucleus frequency across conditions. Data are shown from independent experiments (sgCTRL, $N = 3$; sgTP53, $N = 3$; sg*TP53* + AUGC, $N = 2$; sgTP53 + DRB, $N = 3$; sgTP53 + ActD, $N = 3$). Chi-squared test was used.
(F) Hypertranscription fold change in TCGA tumors from WT-*TP53*/*MDM2* and *TP53*−/*MDM2*+ groups. Each point represents a tumor sample. Mann-Whitney test was used.
(G) Model illustrating how p53 loss induces hypertranscription, nucleotide depletion, replication stress, and genomic instability, leading to chromothripsis and clonal selection through telomere dysfunction and ecDNA amplification. $^{*}p < 0.05$, $^{**}p < 0.01$, $^{***}p < 0.001$, $^{****}p < 0.0001$.
See Figure S14.

gains (Figures 3A–3D).[24] Consistent with LFS tumors, chromothripsis is frequent in LFS fibroblasts and patient tumors,[13,73,74] and *MYC* gain is commonly associated with chromothripsis in LFS.[73] Overall, these primary cultures reproduce key *in vivo* features with high fidelity, although future studies independent of *in vitro* passaging are needed to understand the role of hypertranscription in genomic instability.

RESOURCE AVAILABILITY

Lead contact

Further information and requests for resources and reagents should be directed to and will be fulfilled by the lead contact, Dr. Batsheva Kerem (batshevak@savion.huji.ac.il).

Materials availability

This study did not generate new unique reagents.

Data and code availability

- Raw and processed sequencing data generated in this study have been deposited in EGA: EGAS00001008074.
- The original imaging data, including microscopy images, gels, and immunoblots, have been deposited in Mendeley Data and will be publicly available upon publication (Mendeley Data: https://doi.org/10.17632/nt5nsj9bmf.1).
- This paper does not report any original code.
- Any additional information required to reanalyze the data reported in this paper is available from the lead contact upon request.

ACKNOWLEDGMENTS

The authors thank Maayan Roniger for generating some of the pilot data for this project, Adi Alon for assistance with experimental work, Michalea Hergt and Michele Vousten for excellent technical support, Anne-Sophie Aleixo for support with the ALT-FISH, Axel Benner for advice on the statistical analyses, Gernot Poschet, Glynis Klinke for support with the metabolomics analyses, and the entire Kerem and Ernst research groups for fruitful discussions and ideas. W.Z. acknowledges support from the Neubauer Foundation for the Ph.D. fellowship. This research was partially supported by grants from The European Research Council (starting grant #945674 for U.B.-D.), the cooperation program in Cancer Research of the Deutsches Krebsforschungszentrum (DKFZ), Israel's Ministry of Science and Technology (MOST) to B.K. and A. Ernst, the Israel Cancer Association to B.K., the Israel Science Foundation (grants no. 1284/18 and 1616/24 to B.K.), the ERC (ERC CoG "Unstable Genome" to A. Ernst), and the DFG to A. Ernst.

AUTHOR CONTRIBUTIONS

W.Z. and G.P. designed and performed the vast majority of the experiments and analyzed the data; P.S., S.M., J.O., and M.C. did the computational analyses; M.H. and T. Geiger performed and analyzed the proteomics of BJ cells; F.D. supported the FISH analyses; T. Goldberg and M.I.-T.S. assisted with the combing experiments; K.L. and U.B.-D. generated the control and *TP53* knockout MCF10A cells and contributed to the analysis; A. Eliassaf and O.S. performed and analyzed the metabolomics of BJ cells; K.G. did the strand-seq experiments; G.S. did the proteomics analysis of LFS cells; J.O.K. supervised the strand-seq experiments; J.K. supervised the proteomics analysis of LFS cells; W.Z., G.P., B.K., and A. Ernst wrote the manuscript with input from all authors; B.K. and A. Ernst conceived and supervised the study and secured funding.

DECLARATION OF INTERESTS

The authors declare no competing interests.

DECLARATION OF GENERATIVE AI AND AI-ASSISTED TECHNOLOGIES IN THE WRITING PROCESS

During the preparation of this work, ChatGPT was used during manuscript preparation for language editing. After using this tool, the authors reviewed and edited the content as needed and take full responsibility for the content of the publication. AI was used to create the graphical abstract (Gemini).

STAR★METHODS

Detailed methods are provided in the online version of this paper and include the following:

- KEY RESOURCES TABLE
- METHOD DETAILS
  - Cell culture
  - Growth curves for LFS fibroblasts
  - Population doubling
  - Western blot analysis
  - Quantification of micronuclei and chromatin bridges
  - Immunofluorescence analysis of Phospho Histone 3 (pH3) and Acetyl-alpha-Tubulin and quantification of mitotic defects
  - Immunofluorescence staining for DNA damage markers
  - TERT-FISH
  - ALT FISH
  - Quantification of ecDNAs and ploidy assessment
  - Molecular combing for replication dynamic analysis
  - Telomere length analysis using TeloSizer
  - EU and EdU incorporation assays
  - RNA content analysis using Acridine orange
  - Real-time PCR
  - Metabolomic analysis of fibroblasts from LFS patients
  - Metabolomic analysis of BJ-*hTERT* cells
  - Proteomic analysis of BJ-*hTERT* cells
  - Bulk RNA-sequencing and quantification of gene fusions
  - Sanger sequencing of *TP53* mutation sites in LFS
  - Bulk whole-genome sequencing
  - OncoAnalyser
  - AmpliconSuite
  - Chromothripsis detection
  - Single-cell DNA sequencing by HIPSD-seq and HIPSD&R-seq
  - Strand-seq analysis
  - Analysis of hypertranscription in a public dataset
- QUANTIFICATION AND STATISTICAL ANALYSIS

SUPPLEMENTAL INFORMATION

Supplemental information can be found online at https://doi.org/10.1016/j.molcel.2026.08.003.

Received: July 14, 2025
Revised: April 27, 2026
Accepted: August 4, 2026
Published: September 3, 2026

REFERENCES

1. The ICGC/TCGA Pan-Cancer Analysis of Whole Genomes Consortium (2020). Pan-cancer analysis of whole genomes. Nature *578*, 82–93. https://doi.org/10.1038/s41586-020-1969-6.
2. Stephens, P.J., Greenman, C.D., Fu, B., Yang, F., Bignell, G.R., Mudie, L.J., Pleasance, E.D., Lau, K.W., Beare, D., Stebbings, L.A., et al. (2011). Massive genomic rearrangement acquired in a single catastrophic event during cancer development. Cell *144*, 27–40. https://doi.org/10.1016/j.cell.2010.11.055.

3. Simovic-Lorenz, M., and Ernst, A. (2024). Chromothripsis in cancer. Nat. Rev. Cancer *25*, 79–92. https://doi.org/10.1038/s41568-024-00769-5.

4. Voronina, N., Wong, J.K.L., Hübschmann, D., Hlevnjak, M., Uhrig, S., Heilig, C.E., Horak, P., Kreutzfeldt, S., Mock, A., Stenzinger, A., et al. (2020). The landscape of chromothripsis across adult cancer types. Nat. Commun. *11*, 2320. https://doi.org/10.1038/s41467-020-16134-7.

5. Umbreit, N.T., Zhang, C.-Z., Lynch, L.D., Blaine, L.J., Cheng, A.M., Tourdot, R., Sun, L., Almubarak, H.F., Judge, K., Mitchell, T.J., et al. (2020). Mechanisms generating cancer genome complexity from a single cell division error. Science *368*, eaba0712. https://doi.org/10.1126/science.aba0712.

6. Zhang, C.-Z., Spektor, A., Cornils, H., Francis, J.M., Jackson, E.K., Liu, S., Meyerson, M., and Pellman, D. (2015). Chromothripsis from DNA damage in micronuclei. Nature *522*, 179–184. https://doi.org/10.1038/nature14493.

7. Ly, P., Brunner, S.F., Shoshani, O., Kim, D.H., Lan, W., Pyntikova, T., Flanagan, A.M., Behjati, S., Page, D.C., Campbell, P.J., et al. (2019). Chromosome segregation errors generate a diverse spectrum of simple and complex genomic rearrangements. Nat. Genet. *51*, 705–715. https://doi.org/10.1038/s41588-019-0360-8.

8. Maciejowski, J., Chatzipli, A., Dananberg, A., Chu, K., Toufektchan, E., Klimczak, L.J., Gordenin, D.A., Campbell, P.J., and de Lange, T. (2020). APOBEC3-dependent kataegis and TREX1-driven chromothripsis during telomere crisis. Nat. Genet. *52*, 884–890. https://doi.org/10.1038/s41588-020-0667-5.

9. Crasta, K., Ganem, N.J., Dagher, R., Lantermann, A.B., Ivanova, E.V., Pan, Y., Nezi, L., Protopopov, A., Chowdhury, D., and Pellman, D. (2012). DNA breaks and chromosome pulverization from errors in mitosis. Nature *482*, 53–58. https://doi.org/10.1038/nature10802.

10. Ly, P., Teitz, L.S., Kim, D.H., Shoshani, O., Skaletsky, H., Fachinetti, D., Page, D.C., and Cleveland, D.W. (2017). Selective Y centromere inactivation triggers chromosome shattering in micronuclei and repair by non-homologous end joining. Nat. Cell Biol. *19*, 68–75. https://doi.org/10.1038/ncb3450.

11. Maciejowski, J., Li, Y., Bosco, N., Campbell, P.J., and de Lange, T. (2015). Chromothripsis and Kataegis Induced by Telomere Crisis. Cell *163*, 1641–1654. https://doi.org/10.1016/j.cell.2015.11.054.

12. Waszak, S.M., Northcott, P.A., Buchhalter, I., Robinson, G.W., Sutter, C., Groebner, S., Grund, K.B., Brugières, L., Jones, D.T.W., Pajtler, K.W., et al. (2018). Spectrum and prevalence of genetic predisposition in medulloblastoma: a retrospective genetic study and prospective validation in a clinical trial cohort. Lancet Oncol. *19*, 785–798. https://doi.org/10.1016/S1470-2045(18)30242-0.

13. Rausch, T., Jones, D.T.W., Zapatka, M., Stütz, A.M., Zichner, T., Weischenfeldt, J., Jäger, N., Remke, M., Shih, D., Northcott, P.A., et al. (2012). Genome sequencing of pediatric medulloblastoma links catastrophic DNA rearrangements with TP53 mutations. Cell *148*, 59–71. https://doi.org/10.1016/j.cell.2011.12.013.

14. Mardin, B.R., Drainas, A.P., Waszak, S.M., Weischenfeldt, J., Isokane, M., Stütz, A.M., Raeder, B., Efthymiopoulos, T., Buccitelli, C., Segura-Wang, M., et al. (2015). A cell-based model system links chromothripsis with hyperploidy. Mol. Syst. Biol. *11*, 828. https://doi.org/10.15252/msb.20156505.

15. Muller, P.A.J., and Vousden, K.H. (2014). Mutant p53 in cancer: New functions and therapeutic opportunities. Cancer Cell *25*, 304–317. https://doi.org/10.1016/j.ccr.2014.01.021.

16. Vousden, K.H., and Prives, C. (2009). Blinded by the Light: The Growing Complexity of p53. Cell *137*, 413–431. https://doi.org/10.1016/j.cell.2009.04.037.

17. Menendez, D., Inga, A., and Resnick, M.A. (2009). The expanding universe of p53 targets. Nat. Rev. Cancer *9*, 724–737. https://doi.org/10.1038/nrc2730.

18. Kruiswijk, F., Labuschagne, C.F., and Vousden, K.H. (2015). p53 in survival, death and metabolic health: a lifeguard with a licence to kill. Nat. Rev. Mol. Cell Biol. *16*, 393–405. https://doi.org/10.1038/nrm4007.

19. Roy, S., Tomaszowski, K.-H., Luzwick, J.W., Park, S., Li, J., Murphy, M., and Schlacher, K. (2018). p53 orchestrates DNA replication restart homeostasis by suppressing mutagenic RAD52 and POLθ pathways. eLife *7*, e31723. https://doi.org/10.7554/eLife.31723.

20. Lerner, L.K., Francisco, G., Soltys, D.T., Rocha, C.R.R., Quinet, A., Vessoni, A.T., Castro, L.P., David, T.I.P., Bustos, S.O., Strauss, B.E., et al. (2017). Predominant role of DNA polymerase eta and p53-dependent translesion synthesis in the survival of ultraviolet-irradiated human cells. Nucleic Acids Res. *45*, 1270–1280. https://doi.org/10.1093/nar/gkw1196.

21. Hampp, S., Kiessling, T., Buechle, K., Mansilla, S.F., Thomale, J., Rall, M., Ahn, J., Pospiech, H., Gottifredi, V., and Wiesmüller, L. (2016). DNA damage tolerance pathway involving DNA polymerase ι and the tumor suppressor p53 regulates DNA replication fork progression. Proc. Natl. Acad. Sci. USA *113*, E4311–E4319. https://doi.org/10.1073/pnas.1605828113.

22. Klusmann, I., Rodewald, S., Müller, L., Friedrich, M., Wienken, M., Li, Y., Schulz-Heddergott, R., and Dobbelstein, M. (2016). p53 Activity Results in DNA Replication Fork Processivity. Cell Rep. *17*, 1845–1857. https://doi.org/10.1016/j.celrep.2016.10.036.

23. Yeo, C.Q.X., Alexander, I., Lin, Z., Lim, S., Aning, O.A., Kumar, R., Sangthongpitag, K., Pendharkar, V., Ho, V.H.B., and Cheok, C.F. (2016). p53 Maintains Genomic Stability by Preventing Interference between Transcription and Replication. Cell Rep. *15*, 132–146. https://doi.org/10.1016/j.celrep.2016.03.011.

24. Ernst, A., Jones, D.T.W., Maass, K.K., Rode, A., Deeg, K.I., Jebaraj, B.M.C., Korshunov, A., Hovestadt, V., Tainsky, M.A., Pajtler, K.W., et al. (2016). Telomere dysfunction and chromothripsis. Int. J. Cancer *138*, 2905–2914. https://doi.org/10.1002/ijc.30033.

25. Li, Y., Schwab, C., Ryan, S., Papaemmanuil, E., Robinson, H.M., Jacobs, P., Moorman, A.V., Dyer, S., Borrow, J., Griffiths, M., et al. (2014). Constitutional and somatic rearrangement of chromosome 21 in acute lymphoblastic leukaemia. Nature *508*, 98–102. https://doi.org/10.1038/nature13115.

26. Sanders, A.D., Falconer, E., Hills, M., Spierings, D.C.J., and Lansdorp, P.M. (2017). Single-cell template strand sequencing by Strand-seq enables the characterization of individual homologs. Nat. Protoc. *12*, 1151–1176. https://doi.org/10.1038/nprot.2017.029.

27. Silkworth, W.T., Nardi, I.K., Scholl, L.M., and Cimini, D. (2009). Multipolar spindle pole coalescence is a major source of kinetochore mis-attachment and chromosome mis-segregation in cancer cells. PLOS One *4*, e6564. https://doi.org/10.1371/journal.pone.0006564.

28. Cortés-Ciriano, I., Lee, J.J.-K., Xi, R., Jain, D., Jung, Y.L., Yang, L., Gordenin, D., Klimczak, L.J., Zhang, C.-Z., Pellman, D.S., et al. (2020). Comprehensive analysis of chromothripsis in 2,658 human cancers using whole-genome sequencing. Nat. Genet. *52*, 331–341. https://doi.org/10.1038/s41588-019-0576-7.

29. Otoničar, J., Lazareva, O., Mallm, J.-P., Simovic-Lorenz, M., Philippos, G., Sant, P., Parekh, U., Hammann, L., Li, A., Yildiz, U., et al. (2024). HIPSD&R-seq enables scalable genomic copy number and transcriptome profiling. Genome Biol. *25*, 316. https://doi.org/10.1186/s13059-024-03450-0.

30. Koche, R.P., Rodriguez-Fos, E., Helmsauer, K., Burkert, M., MacArthur, I.C., Maag, J., Chamorro, R., Munoz-Perez, N., Puiggròs, M., Dorado Garcia, H., et al. (2020). Extrachromosomal circular DNA drives oncogenic genome remodeling in neuroblastoma. Nat. Genet. *52*, 29–34. https://doi.org/10.1038/s41588-019-0547-z.

31. Bolkestein, M., Wong, J.K.L., Thewes, V., Körber, V., Hlevnjak, M., Elgaafary, S., Schulze, M., Kommoss, F.K.F., Sinn, H.-P., Anzeneder, T., et al. (2020). Chromothripsis in Human Breast Cancer. Cancer Res. *80*, 4918–4931. https://doi.org/10.1158/0008-5472.CAN-20-1920.

32. Kang, S., Kim, J., Park, A., Koh, M., Shin, W., Park, G., Lee, T.A., Kim, H.J., Han, H., Kim, Y., et al. (2023). TRIM40 is a pathogenic driver of inflammatory bowel disease subverting intestinal barrier integrity. Nat. Commun. *14*, 700. https://doi.org/10.1038/s41467-023-36424-0.

33. Joruiz, S.M., and Bourdon, J.-C. (2016). p53 Isoforms: Key Regulators of the Cell Fate Decision. Cold Spring Harb.. Perspect. Med. *6*, a026039. https://doi.org/10.1101/cshperspect.a026039.

34. Alvarado-Ortiz, E., de la Cruz-López, K.G., Becerril-Rico, J., Sarabia-Sánchez, M.A., Ortiz-Sánchez, E., and García-Carrancá, A. (2020). Mutant p53 Gain-of-Function: Role in Cancer Development, Progression, and Therapeutic Approaches. Front. Cell Dev. Biol. *8*, 607670. https://doi.org/10.3389/fcell.2020.607670.

35. Gottifredi, V., and Wiesmüller, L. (2018). The Tip of an Iceberg: Replication-Associated Functions of the Tumor Suppressor p53. Cancers *10*, 250. https://doi.org/10.3390/cancers10080250.

36. Herrick, J., and Bensimon, A. (1999). Single molecule analysis of DNA replication. Biochimie *81*, 859–871. https://doi.org/10.1016/s0300-9084(99)00210-2.

37. Gorgoulis, V.G., Vassiliou, L.-V.F., Karakaidos, P., Zacharatos, P., Kotsinas, A., Liloglou, T., Venere, M., Ditullio, R.A., Kastrinakis, N.G., Levy, B., et al. (2005). Activation of the DNA damage checkpoint and genomic instability in human precancerous lesions. Nature *434*, 907–913. https://doi.org/10.1038/nature03485.

38. Macheret, M., and Halazonetis, T.D. (2015). DNA replication stress as a hallmark of cancer. Annu. Rev. Pathol. *10*, 425–448. https://doi.org/10.1146/annurev-pathol-012414-040424.

39. Gaillard, H., García-Muse, T., and Aguilera, A. (2015). Replication stress and cancer. Nat. Rev. Cancer *15*, 276–289. https://doi.org/10.1038/nrc3916.

40. Zatzman, M., Fuligni, F., Ripsman, R., Suwal, T., Comitani, F., Edward, L.-M., Denroche, R., Jang, G.H., Notta, F., Gallinger, S., et al. (2022). Widespread hypertranscription in aggressive human cancers. Sci. Adv. *8*, eabn0238. https://doi.org/10.1126/sciadv.abn0238.

41. Ippolito, M.R., Zerbib, J., Eliezer, Y., Reuveni, E., Viganò, S., De Feudis, G., Shulman, E.D., Savir Kadmon, A., Slutsky, R., Chang, T., et al. (2024). Increased RNA and Protein Degradation Is Required for Counteracting Transcriptional Burden and Proteotoxic Stress in Human Aneuploid Cells. Cancer Discov. *14*, 2532–2553. https://doi.org/10.1158/2159-8290.CD-23-0309.

42. Stincone, A., Prigione, A., Cramer, T., Wamelink, M.M.C., Campbell, K., Cheung, E., Olin-Sandoval, V., Grüning, N.-M., Krüger, A., Tauqeer Alam, M., et al. (2015). The return of metabolism: biochemistry and physiology of the pentose phosphate pathway. Biol. Rev. Camb. Philos. Soc. *90*, 927–963. https://doi.org/10.1111/brv.12140.

43. Kanehisa, M., Furumichi, M., Sato, Y., Matsuura, Y., and Ishiguro-Watanabe, M. (2025). KEGG: biological systems database as a model of the real world. Nucleic Acids Res. *53*, D672–D677. https://doi.org/10.1093/nar/gkae909.

44. Ashburner, M., Ball, C.A., Blake, J.A., Botstein, D., Butler, H., Cherry, J.M., Davis, A.P., Dolinski, K., Dwight, S.S., Eppig, J.T., et al. (2000). Gene Ontology: tool for the unification of biology. The Gene Ontology Consortium. Nat. Genet. *25*, 25–29. https://doi.org/10.1038/75556.

45. Gene Ontology Consortium, Aleksander, S.A., Balhoff, J., Carbon, S., Cherry, J.M., Drabkin, H.J., Ebert, D., Feuermann, M., Gaudet, P., Harris, N.L., et al. (2023). The Gene Ontology knowledgebase in 2023. Genetics *224*, iyad031. https://doi.org/10.1093/genetics/iyad031.

46. Milacic, M., Beavers, D., Conley, P., Gong, C., Gillespie, M., Griss, J., Haw, R., Jassal, B., Matthews, L., May, B., et al. (2024). The Reactome Pathway Knowledgebase 2024. Nucleic Acids Res. *52*, D672–D678. https://doi.org/10.1093/nar/gkad1025.

47. Linke, S.P., Clarkin, K.C., Di Leonardo, A., Tsou, A., and Wahl, G.M. (1996). A reversible, p53-dependent G0/G1 cell cycle arrest induced by ribonucleotide depletion in the absence of detectable DNA damage. Genes Dev. *10*, 934–947. https://doi.org/10.1101/gad.10.8.934.

48. Maddocks, O.D.K., Berkers, C.R., Mason, S.M., Zheng, L., Blyth, K., Gottlieb, E., and Vousden, K.H. (2013). Serine starvation induces stress and p53-dependent metabolic remodelling in cancer cells. Nature *493*, 542–546. https://doi.org/10.1038/nature11743.

49. Huang, J., Long, Z., Lin, W., Liao, X., Xie, Y., Liu, L., and Ma, W. (2018). Integrative omics analysis of p53-dependent regulation of metabolism. FEBS Lett. *592*, 380–393. https://doi.org/10.1002/1873-3468.12968.

50. Valente, L.J., Tarangelo, A., Li, A.M., Naciri, M., Raj, N., Boutelle, A.M., Li, Y., Mello, S.S., Bieging-Rolett, K., DeBerardinis, R.J., et al. (2020). p53 deficiency triggers dysregulation of diverse cellular processes in physiological oxygen. J. Cell Biol. *219*, e201908212. https://doi.org/10.1083/jcb.201908212.

51. Anglana, M., Apiou, F., Bensimon, A., and Debatisse, M. (2003). Dynamics of DNA replication in mammalian somatic cells: nucleotide pool modulates origin choice and interorigin spacing. Cell *114*, 385–394. https://doi.org/10.1016/s0092-8674(03)00569-5.

52. Courbet, S., Gay, S., Arnoult, N., Wronka, G., Anglana, M., Brison, O., and Debatisse, M. (2008). Replication fork movement sets chromatin loop size and origin choice in mammalian cells. Nature *455*, 557–560. https://doi.org/10.1038/nature07233.

53. Aird, K.M., Zhang, G., Li, H., Tu, Z., Bitler, B.G., Garipov, A., Wu, H., Wei, Z., Wagner, S.N., Herlyn, M., et al. (2013). Suppression of nucleotide metabolism underlies the establishment and maintenance of oncogene-induced senescence. Cell Rep. *3*, 1252–1265. https://doi.org/10.1016/j.celrep.2013.03.004.

54. Lamm, N., Maoz, K., Bester, A.C., Im, M.M., Shewach, D.S., Karni, R., and Kerem, B. (2015). Folate levels modulate oncogene-induced replication stress and tumorigenicity. EMBO Mol. Med. *7*, 1138–1152. https://doi.org/10.15252/emmm.201404824.

55. Bester, A.C., Roniger, M., Oren, Y.S., Im, M.M., Sarni, D., Chaoat, M., Bensimon, A., Zamir, G., Shewach, D.S., and Kerem, B. (2011). Nucleotide deficiency promotes genomic instability in early stages of cancer development. Cell *145*, 435–446. https://doi.org/10.1016/j.cell.2011.03.044.

56. Broderick, R., Cherdyntseva, V., Nieminuszczy, J., Dragona, E., Kyriakaki, M., Evmorfopoulou, T., Gagos, S., and Niedzwiedz, W. (2023). Pathway choice in the alternative telomere lengthening in neoplasia is dictated by replication fork processing mediated by EXD2's nuclease activity. Nat. Commun. *14*, 2428. https://doi.org/10.1038/s41467-023-38029-z.

57. Lin, C.Y., Lovén, J., Rahl, P.B., Paranal, R.M., Burge, C.B., Bradner, J.E., Lee, T.I., and Young, R.A. (2012). Transcriptional Amplification in Tumor Cells with Elevated c-Myc. Cell *151*, 56–67. https://doi.org/10.1016/j.cell.2012.08.026.

58. Sabò, A., Kress, T.R., Pelizzola, M., de Pretis, S., Gorski, M.M., Tesi, A., Morelli, M.J., Bora, P., Doni, M., Verrecchia, A., et al. (2014). Selective transcriptional regulation by Myc in cellular growth control and lymphomagenesis. Nature *511*, 488–492. https://doi.org/10.1038/nature13537.

59. Ho, J.S.L., Ma, W., Mao, D.Y.L., and Benchimol, S. (2005). p53-Dependent transcriptional repression of c-myc is required for G1 cell cycle arrest. Mol. Cell. Biol. *25*, 7423–7431. https://doi.org/10.1128/MCB.25.17.7423-7431.2005.

60. Porter, J.R., Fisher, B.E., Baranello, L., Liu, J.C., Kambach, D.M., Nie, Z., Koh, W.S., Luo, J., Stommel, J.M., Levens, D., et al. (2017). Global Inhibition with Specific Activation: How p53 and MYC Redistribute the Transcriptome in the DNA Double-Strand Break Response. Mol. Cell *67*, 1013–1025.e9. https://doi.org/10.1016/j.molcel.2017.07.028.

61. Lalonde, M., Trauner, M., Werner, M., and Hamperl, S. (2021). Consequences and Resolution of Transcription-Replication Conflicts. Life (Basel) *11*, 637. https://doi.org/10.3390/life11070637.

62. Lane, A.N., and Fan, T.W.-M. (2015). Regulation of mammalian nucleotide metabolism and biosynthesis. Nucleic Acids Res. *43*, 2466–2485. https://doi.org/10.1093/nar/gkv047.

63. Panatta, E., Butera, A., Mammarella, E., Pitolli, C., Mauriello, A., Leist, M., Knight, R.A., Melino, G., and Amelio, I. (2022). Metabolic regulation by p53 prevents R-loop-associated genomic instability. Cell Rep. *41*, 111568. https://doi.org/10.1016/j.celrep.2022.111568.

64. Merino, D., and Malkin, D. (2014). p53 and hereditary cancer. Subcell. Biochem. *85*, 1–16. https://doi.org/10.1007/978-94-017-9211-0_1.

65. Venkatachalam, S., Shi, Y.P., Jones, S.N., Vogel, H., Bradley, A., Pinkel, D., and Donehower, L.A. (1998). Retention of wild-type p53 in tumors from p53 heterozygous mice: reduction of p53 dosage can promote cancer formation. EMBO J. *17*, 4657–4667. https://doi.org/10.1093/emboj/17.16.4657.

66. Lynch, C.J., and Milner, J. (2006). Loss of one p53 allele results in four-fold reduction of p53 mRNA and protein: a basis for p53 haplo-insufficiency. Oncogene *25*, 3463–3470. https://doi.org/10.1038/sj.onc.1209387.

67. Mannherz, W., and Agarwal, S. (2023). Thymidine nucleotide metabolism controls human telomere length. Nat. Genet. *55*, 568–580. https://doi.org/10.1038/s41588-023-01339-5.

68. Campbell, P.J. (2012). Telomeres and cancer: from crisis to stability to crisis to stability. Cell *148*, 633–635. https://doi.org/10.1016/j.cell.2012.01.043.

69. Smirnov, P., Przybilla, M.J., Simovic-Lorenz, M., Parra, R.G., Susak, H., Ratnaparkhe, M., Wong, J.K., Körber, V., Mallm, J.-P., Philippos, G., et al. (2024). Multi-omic and single-cell profiling of chromothriptic medulloblastoma reveals genomic and transcriptomic consequences of genome instability. Nat. Commun. *15*, 10183. https://doi.org/10.1038/s41467-024-54547-w.

70. Espejo Valle-Inclan, J., De Noon, S., Trevers, K., Elrick, H., van Belzen, I.A.E.M., Zumalave, S., Sauer, C.M., Tanguy, M., Butters, T., Muyas, F., et al. (2025). Ongoing chromothripsis underpins osteosarcoma genome complexity and clonal evolution. Cell *188*, 352–370.e22. https://doi.org/10.1016/j.cell.2024.12.005.

71. Primo, L.M.F., and Teixeira, L.K. (2019). DNA replication stress: oncogenes in the spotlight. Genet. Mol. Biol. *43*, e20190138. https://doi.org/10.1590/1678-4685GMB-2019-0138.

72. Light, N., Layeghifard, M., Attery, A., Subasri, V., Zatzman, M., Anderson, N.D., Hatkar, R., Blay, S., Chen, D., Novokmet, A., et al. (2023). Germline TP53 mutations undergo copy number gain years prior to tumor diagnosis. Nat. Commun. *14*, 77. https://doi.org/10.1038/s41467-022-35727-y.

73. Ratnaparkhe, M., Wong, J.K.L., Wei, P.-C., Hlevnjak, M., Kolb, T., Simovic, M., Haag, D., Paul, Y., Devens, F., Northcott, P., et al. (2018). Defective DNA damage repair leads to frequent catastrophic genomic events in murine and human tumors. Nat. Commun. *9*, 4760. https://doi.org/10.1038/s41467-018-06925-4.

74. Ratnaparkhe, M., Hlevnjak, M., Kolb, T., Jauch, A., Maass, K.K., Devens, F., Rode, A., Hovestadt, V., Korshunov, A., Pastorczak, A., et al. (2017). Genomic profiling of Acute lymphoblastic leukemia in ataxia telangiectasia patients reveals tight link between ATM mutations and chromothripsis. Leukemia *31*, 2048–2056. https://doi.org/10.1038/leu.2017.55.

75. Bischoff, F.Z., Yim, S.O., Pathak, S., Grant, G., Siciliano, M.J., Giovanella, B.C., Strong, L.C., and Tainsky, M.A. (1990). Spontaneous Abnormalities in Normal Fibroblasts from Patients with Li-Fraumeni Cancer Syndrome: Aneuploidy and Immortalization. Cancer Res. *50*, 7979–7984.

76. Laue, K., Pozzi, S., Zerbib, J., Bertolio, R., Eliezer, Y., Cohen-Sharir, Y., Winkler, T., Caputo, M., Ricci, A.A., Adler, L., et al. (2026). p53 inactivation drives breast cancer metastasis to the brain through SCD1 upregulation and increased fatty acid metabolism. Nat. Genet. *58*, 116–131. https://doi.org/10.1038/s41588-025-02446-1.

77. Schindelin, J., Arganda-Carreras, I., Frise, E., Kaynig, V., Longair, M., Pietzsch, T., Preibisch, S., Rueden, C., Saalfeld, S., Schmid, B., et al. (2012). Fiji: an open-source platform for biological-image analysis. Nat. Methods *9*, 676–682. https://doi.org/10.1038/nmeth.2019.

78. Frank, L., Rademacher, A., Mücke, N., Tirier, S.M., Koeleman, E., Knotz, C., Schumacher, S., Stainczyk, S.A., Westermann, F., Fröhling, S., et al. (2022). ALT-FISH quantifies alternative lengthening of telomeres activity by imaging of single-stranded repeats. Nucleic Acids Res. *50*, e61. https://doi.org/10.1093/nar/gkac113.

79. Lebofsky, R., and Bensimon, A. (2003). Single DNA molecule analysis: applications of molecular combing. Brief. Funct. Genomic. Proteomic. *1*, 385–396. https://doi.org/10.1093/bfgp/1.4.385.

80. El-Naggar, A.K. (2004). Concurrent flow cytometric analysis of DNA and RNA. Methods Mol. Biol. *263*, 371–384. https://doi.org/10.1385/1-59259-773-4:371.

81. Liu, Y.-C., Li, F., Handler, J., Huang, C.R.L., Xiang, Y., Neretti, N., Sedivy, J.M., Zeller, K.I., and Dang, C.V. (2008). Global regulation of nucleotide biosynthetic genes by c-Myc. PLOS One *3*, e2722. https://doi.org/10.1371/journal.pone.0002722.

82. Røst, L.M., Shafaei, A., Fuchino, K., and Bruheim, P. (2020). Zwitterionic HILIC tandem mass spectrometry with isotope dilution for rapid, sensitive and robust quantification of pyridine nucleotides in biological extracts. J. Chromatogr. B Analyt. Technol. Biomed. Life Sci. *1144*, 122078. https://doi.org/10.1016/j.jchromb.2020.122078.

83. Mackay, G.M., Zheng, L., van den Broek, N.J.F., and Gottlieb, E. (2015). Analysis of Cell Metabolism Using LC-MS and Isotope Tracers. Methods Enzymol. *561*, 171–196. https://doi.org/10.1016/bs.mie.2015.05.016.

84. Geiger, T., Wisniewski, J.R., Cox, J., Zanivan, S., Kruger, M., Ishihama, Y., and Mann, M. (2011). Use of stable isotope labeling by amino acids in cell culture as a spike-in standard in quantitative proteomics. Nat. Protoc. *6*, 147–157. https://doi.org/10.1038/nprot.2010.192.

85. Geiger, T., Cox, J., Ostasiewicz, P., Wisniewski, J.R., and Mann, M. (2010). Super-SILAC mix for quantitative proteomics of human tumor tissue. Nat. Methods *7*, 383–385. https://doi.org/10.1038/nmeth.1446.

86. Wiśniewski, J.R., Zougman, A., Nagaraj, N., and Mann, M. (2009). Universal sample preparation method for proteome analysis. Nat. Methods *6*, 359–362. https://doi.org/10.1038/nmeth.1322.

87. Wiśniewski, J.R., Zougman, A., and Mann, M. (2009). Combination of FASP and StageTip-based fractionation allows in-depth analysis of the hippocampal membrane proteome. J. Proteome Res. *8*, 5674–5678. https://doi.org/10.1021/pr900748n.

88. Rappsilber, J., Mann, M., and Ishihama, Y. (2007). Protocol for micro-purification, enrichment, pre-fractionation and storage of peptides for proteomics using StageTips. Nat. Protoc. *2*, 1896–1906. https://doi.org/10.1038/nprot.2007.261.

89. Michalski, A., Damoc, E., Hauschild, J.-P., Lange, O., Wieghaus, A., Makarov, A., Nagaraj, N., Cox, J., Mann, M., and Horning, S. (2011). Mass spectrometry-based proteomics using Q Exactive, a high-performance benchtop quadrupole Orbitrap mass spectrometer. Mol. Cell. Proteomics *10*, M111.011015. https://doi.org/10.1074/mcp.M111.011015.

90. Cox, J., Neuhauser, N., Michalski, A., Scheltema, R.A., Olsen, J.V., and Mann, M. (2011). Andromeda: a peptide search engine integrated into the MaxQuant environment. J. Proteome Res. *10*, 1794–1805. https://doi.org/10.1021/pr101065j.

91. Tusher, V.G., Tibshirani, R., and Chu, G. (2001). Significance analysis of microarrays applied to the ionizing radiation response. Proc. Natl. Acad. Sci. USA *98*, 5116–5121. https://doi.org/10.1073/pnas.091062498.

92. DKFZ-ODCF. (2024). (DKFZ - ODCF)/RNAseqWorkflow.

93. DKFZ-ODCF. (2024). DKFZ-ODCF/AlignmentAndQCWorkflows.

94. The Roddy Workflow Management System. (2024). TheRoddyWMS/Roddy-Default-Plugin.

95. The Roddy Workflow Management System. (2024). TheRoddyWMS/Roddy-Base-Plugin.

96. The Roddy Workflow Management System. (2024). TheRoddyWMS/Roddy.

97. Dobin, A., Davis, C.A., Schlesinger, F., Drenkow, J., Zaleski, C., Jha, S., Batut, P., Chaisson, M., and Gingeras, T.R. (2013). STAR: ultrafast universal RNA-seq aligner. Bioinformatics *29*, 15–21. https://doi.org/10.1093/bioinformatics/bts635.

98. Tarasov, A., Vilella, A.J., Cuppen, E., Nijman, I.J., and Prins, P. (2015). Sambamba: fast processing of NGS alignment formats. Bioinformatics *31*, 2032–2034. https://doi.org/10.1093/bioinformatics/btv098.

99. Li, H., Handsaker, B., Wysoker, A., Fennell, T., Ruan, J., Homer, N., Marth, G., Abecasis, G., and Durbin, R.; 1000 Genome Project Data Processing Subgroup (2009). The Sequence Alignment/Map format and SAMtools. Bioinformatics *25*, 2078–2079. https://doi.org/10.1093/bioinformatics/btp352.

100. DeLuca, D.S., Levin, J.Z., Sivachenko, A., Fennell, T., Nazaire, M.-D., Williams, C., Reich, M., Winckler, W., and Getz, G. (2012). RNA-SeQC: RNA-seq metrics for quality control and process optimization. Bioinformatics *28*, 1530–1532. https://doi.org/10.1093/bioinformatics/bts196.

101. Liao, Y., Smyth, G.K., and Shi, W. (2014). featureCounts: an efficient general purpose program for assigning sequence reads to genomic features. Bioinformatics *30*, 923–930. https://doi.org/10.1093/bioinformatics/btt656.

102. Uhrig, S., Ellermann, J., Walther, T., Burkhardt, P., Fröhlich, M., Hutter, B., Toprak, U.H., Neumann, O., Stenzinger, A., Scholl, C., et al. (2021). Accurate and efficient detection of gene fusions from RNA sequencing data. Genome Res. *31*, 448–460. https://doi.org/10.1101/gr.257246.119.

103. Tarazona, S., Furió-Tarí, P., Turrà, D., Pietro, A.D., Nueda, M.J., Ferrer, A., and Conesa, A. (2015). Data quality aware analysis of differential expression in RNA-seq with NOISeq R/Bioc package. Nucleic Acids Res. *43*, e140. https://doi.org/10.1093/nar/gkv711.

104. Tarazona, S., García-Alcalde, F., Dopazo, J., Ferrer, A., and Conesa, A. (2011). Differential expression in RNA-seq: a matter of depth. Genome Res. *21*, 2213–2223. https://doi.org/10.1101/gr.124321.111.

105. Wu, T., Hu, E., Xu, S., Chen, M., Guo, P., Dai, Z., Feng, T., Zhou, L., Tang, W., Zhan, L., et al. (2021). clusterProfiler 4.0: A universal enrichment tool for interpreting omics data. Innovation (Camb) *2*, 100141. https://doi.org/10.1016/j.xinn.2021.100141.

106. Bioconductor (2025). org.Hs.eg.db Bioconductor. http://bioconductor.org/packages/org.Hs.eg.db/.

107. Wickham, H., Chang, W., Henry, L., Lin Pedersen, T., Wilke, C., Woo, K., Yutani, H., Dunnington, D., and van den Brand, T. (2016). Create Elegant Data Visualisations Using the Grammar of Graphics. https://ggplot2.tidyverse.org/.

108. Kolde, R. (2019). pheatmap: Pretty Heatmaps, [Version 1.0.12].

109. Reisinger, E., Genthner, L., Kerssemakers, J., Kensche, P., Borufka, S., Jugold, A., Kling, A., Prinz, M., Scholz, I., Zipprich, G., et al. (2017). OTP: An automatized system for managing and processing NGS data. J. Biotechnol. *261*, 53–62. https://doi.org/10.1016/j.jbiotec.2017.08.006.

110. GitHub. (2025). Home GitHub. https://github.com/DKFZ-ODCF/AlignmentAndQCWorkflows/wiki/Home.

111. 1000 Genomes Project Consortium, Auton, A., Brooks, L.D., Durbin, R.M., Garrison, E.P., Kang, H.M., Korbel, J.O., Marchini, J.L., McCarthy, S., McVean, G.A., et al. (2015). A global reference for human genetic variation. Nature *526*, 68–74. https://doi.org/10.1038/nature15393.

112. Li, H. (2013). Aligning Sequence Reads, Clone Sequences and Assembly Contigs with BWA-MEM. Preprint at arXiv. https://doi.org/10.48550/arXiv.1303.3997.

113. Broad Institute. (2024). broadinstitute/picard.

114. Danecek, P., Bonfield, J.K., Liddle, J., Marshall, J., Ohan, V., Pollard, M.O., Whitwham, A., Keane, T., McCarthy, S.A., Davies, R.M., et al. (2021). Twelve years of SAMtools and BCFtools. GigaScience *10*, giab008. https://doi.org/10.1093/gigascience/giab008.

115. Oncoanalyser: Introduction https://nf-co.re/oncoanalyser/dev.html.

116. hmftools/linx/README.md at master · hartwigmedical/hmftools · GitHub https://github.com/hartwigmedical/hmftools/blob/master/linx/README.md.

117. Cameron, D.L., Baber, J., Shale, C., Valle-Inclan, J.E., Besselink, N., van Hoeck, A., Janssen, R., Cuppen, E., Priestley, P., and Papenfuss, A.T. (2021). GRIDSS2: comprehensive characterisation of somatic structural variation using single breakend variants and structural variant phasing. Genome Biol. *22*, 202. https://doi.org/10.1186/s13059-021-02423-x.

118. hmftools/purple/README.md at master · hartwigmedical/hmftools · GitHub https://github.com/hartwigmedical/hmftools/blob/master/purple/README.md.

119. Luebeck, J., Huang, E., Kim, F., Liefeld, T., Dameracharla, B., Ahuja, R., Schreyer, D., Prasad, G., Adamaszek, M., Kenkre, R., et al. (2024). AmpliconSuite: an end-to-end workflow for analyzing focal amplifications in cancer genomes. Preprint at bioRxiv. https://doi.org/10.1101/2024.05.06.592768.

120. Talevich, E., Shain, A.H., Botton, T., and Bastian, B.C. (2016). CNVkit: Genome-Wide Copy Number Detection and Visualization from Targeted DNA Sequencing. PLOS Comput. Biol. *12*, e1004873. https://doi.org/10.1371/journal.pcbi.1004873.

121. Olshen, A.B., Venkatraman, E.S., Lucito, R., and Wigler, M. (2004). Circular binary segmentation for the analysis of array-based DNA copy number data. Biostatistics *5*, 557–572. https://doi.org/10.1093/biostatistics/kxh008.

122. Deshpande, V., Luebeck, J., Nguyen, N.D., Bakhtiari, M., Turner, K.M., Schwab, R., Carter, H., Mischel, P.S., and Bafna, V. (2019). Exploring the landscape of focal amplifications in cancer using AmpliconArchitect. Nat. Commun. *10*, 392. https://doi.org/10.1038/s41467-018-08200-y.

123. Espejo Valle-Inclán, J., and Cortés-Ciriano, I. (2023). ReConPlot: an R package for the visualization and interpretation of genomic rearrangements. Bioinformatics *39*, btad719. https://doi.org/10.1093/bioinformatics/btad719.

124. Seufert, I., Sant, P., Bauer, K., Syed, A.P., Rippe, K., and Mallm, J.-P. (2023). Enhancing sensitivity and versatility of Tn5-based single cell omics. Front. Epigenet. Epigenom. *1*. https://doi.org/10.3389/freae.2023.1245879.

125. ShahCompBio. (2024). shahcompbio/hmmcopy_utils.

126. Bioconductor (2025). HMMcopy Bioconductor. http://bioconductor.org/packages/HMMcopy/.

127. Gu, Z., Eils, R., and Schlesner, M. (2016). Complex heatmaps reveal patterns and correlations in multidimensional genomic data. Bioinformatics *32*, 2847–2849. https://doi.org/10.1093/bioinformatics/btw313.

128. Lawrence, M., Huber, W., Pagès, H., Aboyoun, P., Carlson, M., Gentleman, R., Morgan, M.T., and Carey, V.J. (2013). Software for Computing and Annotating Genomic Ranges. PLOS Comput. Biol. *9*, e1003118. https://doi.org/10.1371/journal.pcbi.1003118.

129. Sanders, A.D., Meiers, S., Ghareghani, M., Porubsky, D., Jeong, H., van Vliet, M.A.C.C., Rausch, T., Richter-Pechańska, P., Kunz, J.B., Jenni, S., et al. (2020). Single-cell analysis of structural variations and complex rearrangements with tri-channel processing. Nat. Biotechnol. *38*, 343–354. https://doi.org/10.1038/s41587-019-0366-x.

CellPress
OPEN ACCESS

STAR★METHODS

KEY RESOURCES TABLE

REAGENT or RESOURCE	SOURCE	IDENTIFIER
Antibodies		
Phospho-Histone H3 (Ser10) (6G3) Mouse mAb	Cell Signaling Technology	Cat# 9706; RRID: AB_331748
Acetyl-α-Tubulin (Lys40) (D20G3) XP Rabbit mAb	Cell Signaling Technology	Cat# 5335; RRID: AB_10544694
Anti-Digoxigenin-Rhodamine (Fab fragments)	Roche	Cat# 11207750910; RRID:AB_514501
Mouse monoclonal Anti-p53 antibody	Sigma-Aldrich	Cat# P6874; RRID: AB_1079545
Mouse anti-β-catenin	BD Biosciences	Cat# 610153; RRID: AB_397554
Peroxidase-AffiniPure Donkey Anti-Rabbit IgG (H+L)	Jackson ImmunoResearch Labs	Cat# 711-035-152; RRID: AB_10015282
Anti-phospho-Histone H2A.X (Ser139) Antibody, clone JBW301	Millipore	Cat# 05-636-I; RRID: AB_2755003
Rabbit anti-53BP1 Antibody, Affinity Purified	Bethyl Laboratories	Cat# A300-272A; RRID: AB_185520
Anti-BrdU antibody [BU1/75 (ICR1)] – Proliferation Marker	abcam	Cat# ab6326; RRID: AB_305426
Purified Mouse Anti-BrdU Clone B44	BD Biosciences	Cat# BD347580; RRID: AB_10015219
AffiniPure® Donkey Anti-Mouse IgG (H+L	Jackson ImmunoResearch Laboratories	Cat# 715-035-150; RRID: AB_2340770
Goat anti-mouse Alexa Fluor 488	Invitrogen	Cat# A11001; RRID: AB_2534069
Goat anti-rat Alexa Fluor 594	Invitrogen	Cat# A11007; RRID: AB_10561522
Mouse anti-ssDNA	Millipore	Cat# MAB3034; RRID: AB_11212688
Donkey anti-mouse Alexa Fluor 647	Invitrogen	Cat# A31571; RRID: AB_162542
Chemicals, peptides, and recombinant proteins		
Minimum Essential Medium (MEM) Eagle	Sigma-Aldrich	Cat# M5650
DMEM/F-12, HEPES	Gibco	Cat# 31330038
Phosphate buffer solution	Sigma-Aldrich	Cat# P5244
Fetal Bovine Serum, Value	Gibco	Cat# A5256701
Horse Serum	Sigma-Aldrich	Cat# H1270
Puromycin	invivogen	Cat# ant-pr-1
GlutaMAX supplement	Gibco	Cat# 35050038
Penicillin-Streptomycin (10,000 U/mL)	Gibco	Cat# 15140122
Trypsin-EDTA solution	Sigma-Aldrich	Cat# T4049
Epidermal Growth Factor, human	Sigma-Aldrich	Cat# E9644
Hydrocortisone	Sigma-Aldrich	Cat# H0888
Insulin solution from bovine pancreas	Sigma-Aldrich	Cat# I0516
Cholera Toxin	Sigma-Aldrich	Cat# C8052
Transferrin human	Sigma-Aldrich	Cat# T8158
DAPI Fluoromount-G Mounting Medium	Southern Biotechnology	Cat# 0100-20
Triton X-100	Sigma-Aldrich	Cat# 93443
DNA *TERT* probe (Clone RP11-117B23)	Source BioScience	Clone RP11-117B23
Digoxigenin-11-dUTP	Roche	Cat# 1570013
Cot-1 DNA	Life Technologies	Cat# 15279-011
Herring Sperm DNA	Thermo Fisher Scientific	Cat# 15634017
VECTASHIELD Vibrance Antifade Mounting Medium with DAPI	Vector Laboratories	Cat# H-1800
TelC probe, 5′-Atto594-(CCCTAA)5-3′	Eurofins Genomics	Custom oligo

(*Continued on next page*)

Continued

REAGENT or RESOURCE	SOURCE	IDENTIFIER
BrdU	Sigma-Aldrich	Cat# B5002
5-iodo-2′-deoxyuridine (IdU)	Sigma-Aldrich	Cat# I7125
5-chloro-2deoxyurdine (CldU)	Sigma-Aldrich	Cat# C6891
NP-40 (Igepal substitute, Strand-seq buffer)	Sigma-Aldrich	Cat# 74385
Hoechst 33258	Enzo Life Sciences	Cat# ENZ-52402
Methanol-free formaldehyde (1.5%)	Thermo Fisher Scientific	Cat# 28906
Protease inhibitor cocktail	Cell Signaling Technology	Cat# 5871S
NEBuffer 2.1	NEB	Cat# B7202
SDS	Serva	Cat# 20767
RNase inhibitor	Takara Bio	Cat# 2313A
Micrococcal Nuclease (MNase)	NEB	Cat# M0247S
DTT	Sigma-Aldrich	Cat# 43816
PEG 6000	Calbiochem	Cat# 528877
T4 DNA polymerase	NEB	Cat# M0203S
Klenow DNA polymerase	NEB	Cat# M0210S
T4 polynucleotide kinase	NEB	Cat# M0201S
T4 ligase buffer	NEB	Cat# B0202S
dNTP mix (2 mM)	NEB	Cat# N0447S
Klenow Fragment (3′→5′ exo−)	NEB	Cat# M0212S
dATP (1.67 mM)	NEB	Cat# N0440S
Quick Ligase (with buffer)	NEB	Cat# M2200L
Phusion HF PCR Master Mix	NEB	Cat# M0531L
Illumina PE adaptor-1 and PE adaptor-2 (custom oligos)	Custom synthesis	Sequences in STAR Methods text
Custom multiplexing Primer PE 2.0 and Primer PE 1.0 (custom oligos)	Sigma-Aldrich / Illumina	Sequences in STAR Methods text
Amersham™ ECL™ Select Western blot detection reagent	Cytiva	Cat# RPN2235
YOYO™-1 Iodide (491/509)	Thermo Fisher Scientific	Cat# Y3601
Adenosine	Sigma-Aldrich	Cat# A9251
Uridine	Sigma-Aldrich	Cat# U3750
Cytidine	Sigma-Aldrich	Cat# C122106
Guanosine	Sigma-Aldrich	Cat# G6752
Nutlin-3a	Sigma-Aldrich	Cat# SML0580
Ribonuclease A from bovine pancreas	Sigma-Aldrich	Cat# R6513
Deoxyribonuclease I from bovine pancreas	Sigma-Aldrich	Cat# DN25
5,6-Dichlorobenzimidazole 1-β-D-ribofuranoside(DRB)	Sigma-Aldrich	Cat# D1916
Actinomycin D	Sigma-Aldrich	Cat# A9415-2MG
Acridine Orange	Sigma-Aldrich	Cat# A6014
Critical commercial assays		
AllPrep DNA/RNA/Protein Mini Kit	QIAGEN	Cat# 80004
Agilent RNA 6000 Pico Kit (Bioanalyzer)	Agilent	Cat# 5067-1513
Qubit RNA BR Assay Kit	Thermo Fisher Scientific	Cat# Q10211
TapeStation RNA ScreenTape assay	Agilent Technologies	Cat# 5067-5576, 5067–5577
DNeasy Blood & Tissue Kit	QIAGEN	Cat# 69504
Qubit dsDNA HS Assay Kit	Life Technologies	Cat# Q32851
Agilent High Sensitivity DNA Kit (Bioanalyzer)	Agilent	Cat# 5067-4626
Qubit dsDNA BR Assay Kit	Thermo Fisher Scientific	Cat# Q32853

(*Continued on next page*)

Continued

REAGENT or RESOURCE	SOURCE	IDENTIFIER
TapeStation Genomic DNA ScreenTape assay	Agilent Technologies	Cat# 5067-5365, 5067–5366
Chromium Next GEM Chip H	10x Genomics	Cat# PN-1000161
Chromium Next GEM Single Cell ATAC Library & Gel Bead Kit v1.1	10x Genomics	Cat# PN-1000176
Single Index Kit N Set A	10x Genomics	Cat# PN-1000212
Chromium Next GEM Chip J	10x Genomics	Cat# PN-1000230
Chromium Next GEM Single Cell Multiome ATAC + Gene Expression Reagent Bundle	10x Genomics	Cat# PN-1000285
Dual Index Kit TT Set A	10x Genomics	Cat# PN-1000215
AMPure XP beads	Beckman Coulter	Cat# A63881
TheraPEAK ProFreeze Freezing Medium	Lonza	Cat# BEBP12-769E
Fiber-Prep kit	Genomic Vision	Cat# EXTR-001
Fiber-Comb kit	Genomic Vision	Cat# MSC-001
Click-iT RNA Imaging Kit	Invitrogen	Cat# C10329 and C10330
RNeasy Mini Kit	QIAGEN	Cat# 74104
High Capacity cDNA Reverse Transcription Kit	Thermo Fisher Scientific	Cat# 4368814
Platinum™ SuperFi II PCR Master Mixes	Invitrogen	Cat# 12369010
Power SYBR™ Green PCR Master Mix	Thermo Fisher Scientific	Cat# 4367659
Experimental models: Cell lines		
LFS041 (Li-Fraumeni Syndrome patient-derived skin fibroblasts)	Michael A. Tainsky (Detroit, USA)	Patient-derived; multiple passages (early/ crisis/ post-crisis/ late)
LFS087 (Li-Fraumeni Syndrome patient-derived skin fibroblasts)	Michael A. Tainsky (Detroit, USA)	Patient-derived; multiple passages (early/post-crisis/late)
LFS174 (Li-Fraumeni Syndrome patient-derived skin fibroblasts)	Michael A. Tainsky (Detroit, USA)	Patient-derived; multiple passages (crisis)
LFS8 (healthy donor skin fibroblasts, family of LFS041)	Michael A. Tainsky (Detroit, USA)	Healthy control fibroblasts
LFS9 (healthy donor skin fibroblasts, family of LFS041)	Michael A. Tainsky (Detroit, USA)	Healthy control fibroblasts
BJ-*hTERT* cells	Clontech	Cat# 6332102
MCF10A cells	ATCC	not available
Recombinant DNA		
pRS-Shp53-puro	Professor R. Agami.	not available
pRS-shRNA-puro	Professor R. Agami.	not available
sgRNA-*TP53*	Integrated DNA Technologies	sgRNA1 CGCTATCTGAGCA GCGCTCATGGsgRNA2 CCC CGGACGATATTGAACAA
sgRNA-LacZ	Integrated DNA Technologies	sgRNA1AACGGCGGATTGA CCGTAATsgRNA2CTAACG CCTGGGTCGAACG
Deposited data		
Source data for figures: original microscopy images and uncropped, uprocessed gels and immunoblots	This study	Mendeley Data: https://doi.org/10.17632/nt5nsj9bmf.1
All raw and processed sequencing data	This study	EGA: EGAS00001008074
Software and algorithms		
ZEN 3.0 Microscopy Software (Blue Edition)	Zeiss	v3.0
ZEN 2.3 Microscopy Software (Blue Edition)	Zeiss	v2.3
Microsoft Excel (Microsoft Office 365)	Microsoft	v2501
ImageJ (FIJI)	National Institutes of Health (NIH)	v1.54f

(*Continued on next page*)

Continued

REAGENT or RESOURCE	SOURCE	IDENTIFIER
GraphPad Prism	GraphPad Software	v8 / v10
LAS X Software	Leica Microsystems	v3.7.6
Analyst	AB SCIEX	v1.7.2
OS software suite	AB SCIEX	v2.0.0
R Studio	Posit (formerly RStudio) (accessed via DKFZ ODCF Cluster)	v4.3.0
Python	Python Software Foundation (accessed via DKFZ ODCF Cluster)	v3.10.14
AmpliconSuite	UC San Diego / AmpliconSuite Team	v1.2.2
Cell Ranger ATAC pipeline	10x Genomics	v2.1.0
Cell Ranger DNA pipeline (bamsplice)	10x Genomics	v1.1.0
MosaiCatcher pipeline	European Molecular Biology Laboratory (EMBL)	v2.0.1
MetaboAnalyst	MetaboAnalyst	v6.0
MosaiClassifier	European Molecular Biology Laboratory (EMBL)	Part of MosaiCatcher v2.0.1
Cell Ranger Arc reference (GRCh38)	10x Genomics	v2020-A
Affinity Designer 2	Serif	v2.5.5
Zotero	Corporation for Digital Scholarship	v7.0.11
BioRender	BioRender Inc.	not applicable

METHOD DETAILS

Cell culture

LFS fibroblasts

Skin-derived fibroblasts from Li-Fraumeni Syndrome patients (cells were kindly provided by Michael A. Tainsky) were grown in Minimum Essential Medium (MEM) Eagle (Sigma; M5650), supplemented with 10% fetal calf serum, 1% glutamine and 1% penicillin/streptomycin and cultured in 60 mm cell culture dishes (Falcon, #353004) at 37°C with 5% CO2. Cells from two LFS patients were used, namely patients LFS041 and LFS087. The classification of cells into early passage cells, crisis cells and late passage cells was based on well-defined criteria related to the growth speed (doubling time, split ratios, slope of the growth curve, see Figures 1A and S1A) and the morphology of the cells (see Figures 1A and S1). These canonical classification criteria of the time points were already used in previous studies for these cells.[75] On average, early-passage cells were passaged once a week using 0.025% Trypsin/EDTA for trypsinization, post-crisis and late-passage cells twice a week, while crisis-passage cells took several weeks per passage to reach confluency. Fibroblasts from patients LFS8 and LFS9 (skin-derived fibroblasts from healthy individuals the same family as LFS041) were grown in MEM alpha, supplemented with 15% fetal calf serum, 1% glutamine and 1% penicillin/streptomycin. STR profiling was conducted to authenticate the cells using a multiplex PCR-based method provided by Multiplexion. The analysis confirmed the cultures' uniqueness and the absence of cross-contamination with other cell lines. Furthermore, the cells were confirmed to be mycoplasma-free using a PCR-based assay provided by Eurofins. Cell morphology was imaged using a Zeiss Axio Vert.A1 inverted microscope at 5X magnification. ZEN 3.0 Microscopy Software was used for image processing.

BJ fibroblasts

BJ-*hTERT* normal human fibroblast cells were grown in Dulbecco's modified Eagle's medium (DMEM) supplemented with 10% Fetal bovine serum (FBS), 100,000 U/l penicillin and 100 mg/l streptomycin. The nucleosides-supplemented media was prepared by adding 50μM of each nucleoside A, U, C and G from sigma. For p53 downregulation experiment, Bj-*hTERT* cells were infected by vectors expressing short-hairpin RNA against p53 mRNA as follows: Phoenix retroviral packaging cells were transiently transfected with plasmids, then the BJ-*hTERT* cells were infected three times with Phoenix cell supernatant containing defective viruses and 10 mg/ml polybrene. Following the infection, the cells were selected using selection reagents Puromycin for up to 7-10 days. The vectors are pRS-Shp53-puro (p53 downregulation) and pRS-shRNA-puro (scrambled shRNA as a control), kindly received from Professor R. Agami.

MCF10A epithelial cells

MCF10A, immortalized human breast epithelial cell line carrying sgLacZ control (sgCTRL) or sg*TP53* constructs (generated using two guide RNAs targeting *TP53*), were generated as described.[76] Briefly, target sequences were cloned into a lentiCRISPRv2 vector, constructs were validated by Sanger sequencing, lentiviral particles were produced in HEK293T cells using a third-generation system and used to infect the MCF10A cells (8 μg ml−1 polybrene), followed by antibiotics selection. p53 deficiency was validated by

quantitative PCR. Cells were cultured as previously described.[76] Briefly, cells were grown in DMEM/F12 supplemented with 5% horse serum, 1% penicillin/streptomycin, 20 ng/mL epidermal growth factor (EGF), 0.5 μg/mL hydrocortisone, 10 μg/mL insulin, 100 ng/mL cholera toxin, and 2.5 μg/mL transferrin. Cells were maintained under standard conditions at 37°C and 5% CO_2

Growth curves for LFS fibroblasts

The time required to reach confluency was used as a proxy for the growth characteristics. In the growth curve graphs, the splitting ratio used at each passage is indicated for the corresponding passage number. A shorter time to reach confluency at specific passages suggests increased growth rates, while longer times indicate slower growth, reflecting changes in cell population dynamics. Graphs were generated using Microsoft Excel.

Population doubling

Primary LFS cells grow in cell culture conditions as mentioned. The initial number of the cells were counted and determined, after several days the cells were trypsinized, counted and passaged by 1:2 ratio. The population doubling (PDL) for each passage calculated as PDL = 3.32 (log (Final cell number) - log (Initial cell number)). The sum of PDLs gives the cumulative population curve.

Western blot analysis

Sample buffer was used for protein extraction. The extracted protein is loaded in 12% polyacrylamide gel, separated in 100m Volt for 50 min. The gel was transferred to a nitrocellulose membrane and blocked with 8% milk. The antibody hybridization and chemiluminescence (ECL) were performed according to standard procedures. The primary antibodies used are DO-1 (1:5000) from sigma for p53 detection, and mouse anti β-catenin (1:2,500) from BD-Biosciences. HRP-conjugated anti-mouse and anti rabbit was obtained from Jackson ImmunoResearch Laboratories (711-035-152, 1:5000).

Quantification of micronuclei and chromatin bridges

Cells were seeded on coverslips in 6-well plates and fixed with 4% PFA at pH 6.8 for 15 minutes. Following fixation, the cells were washed twice with 1X PBS for 5 minutes, rinsed in double distilled water and then in absolute ethanol. The coverslips were air-dried at room temperature before being mounted on slides (Thermo Fisher Scientific, #J1800AMNZ) using DAPI Fluoromount-G Mounting Medium (Southern Biotechnology, #0100-20) and left to solidify in the dark at room temperature for 1 hour. Cell imaging and quantifications were performed using Zeiss AXIO imager 2. ZEN 2.3 Microscopy Software was used for data acquisition, while ZEN 3.0 Microscopy Software and ImageJ 1.54f were used for image processing. Micronuclei and chromatin bridges (defined as small, extranuclear bodies containing chromatin that appear as separate, round DAPI-stained DNA fragments near the main nucleus, and as continuous strands of DNA connecting two daughter nuclei during or after cell division, visible as thin DAPI-stained threads spanning the space between nuclei, respectively) from 750 cells from at least three biological replicates per passage were quantified. GraphPad Prism 8 software was used to create graphs, perform statistical tests and calculate p values. Statistical significance was assessed using a one-way ANOVA followed by Tukey's multiple comparisons test, with p values below 0.05 considered as statistically significant ($^{*}p < 0.05$, $^{**}p < 0.01$, $^{***}p < 0.001$, $^{****}p < 0.0001$).

Immunofluorescence analysis of Phospho Histone 3 (pH3) and Acetyl-alpha-Tubulin and quantification of mitotic defects

Cells were seeded on coverslips in 6-well plates and allowed to reach 60-70% confluency. Once confluency was achieved, the coverslips were rinsed with cell wash PBS (1X PBS, 1% of 1M MgCl2) and the cells were fixed with 4% PFA at pH 6.8 for 15 minutes. Following fixation, the cells were washed twice with 50mM NH4Cl for 5 minutes each, and twice with 1X PBS with rocking. Next, a freshly prepared blocking buffer (1X PBS, 5% normal goat serum, 0.3% Triton X-100) was added to the coverslips and incubated for 1 hour at room temperature. After removing the blocking buffer, a mixture of primary antibodies – Phospho-Histone H3 (Ser10) (6G3) mouse mAb (Cell Signaling, #9706, Lot#10) diluted at 1:400 and Acetyl-α-Tubulin (Lys40) (D20G3) XP rabbit mAb (Cell Signaling, #5335, Lot #5) diluted at 1:800 – was added to each coverslip in an antibody dilution buffer (1X PBS, 1% BSA, 0.3% Triton X-100). The coverslips were then incubated overnight at 4°C. The next day, the coverslips were washed once with 1X PBS for 45 minutes and twice for 15 minutes. A secondary antibody mix consisting of goat anti-mouse and goat anti-rabbit antibodies, both diluted at 1:1000 in antibody dilution buffer, was applied to each coverslip and incubated in the dark for 90 minutes at room temperature. Subsequently, the coverslips were washed three times for 15 minutes in 1X PBS, rinsed in ddH2O, and then in absolute ethanol. Finally, the coverslips were air-dried at room temperature before being mounted on slides using DAPI Fluoromount-G Mounting Medium and left to solidify in the dark at room temperature for 1 hour. Cell imaging and quantification were performed using a Zeiss AXIO Imager 2 with ZEN 2.3 Microscopy Software. Representative images were captured using a Leica SP8 confocal microscope. Maximum intensity projections were applied using LAS X software, and further image processing was performed with both LAS X software and ImageJ 1.54f. A total of 100 cells per patient and per biological replicate across three independent replicates were quantified. GraphPad Prism 8 software was utilized to create graphs, perform statistical tests, and calculate p values. Statistical significance was assessed using repeated-measures two-way ANOVA followed by uncorrected Fisher's LSD for multiple comparisons; p values below 0.05 were considered statistically significant ($N = 3$ per group; $^{*}p < 0.05$, $^{**}p < 0.01$, $^{***}p < 0.001$, $^{****}p < 0.0001$).

Immunofluorescence staining for DNA damage markers

Cells were fixed in 3.7% formaldehyde/PBS for 10 min, permeabilized with 0.5% Triton/PBS for 10 min, and blocked with 3% BSA/PBS for 1 hour. The primary antibodies used were mouse anti-phosphorylated H2AX (Milipore, 1:100), rabbit anti-53BP1 (Bethyl Laboratories, 1:100) and incubated overnight in 4c. The secondary antibodies used were anti-mouse Alexa Fluor 488 (Invitrogen), anti-rabbit Alexa fluor 546 (Abcam). DNA was counterstained with a mounting medium for fluorescence with DAPI (Vector Laboratories). Images were analyzed for foci and micronuclei formation double blindly using Fiji.[77]

TERT-FISH

50,000 cells in supplemented MEM were seeded on a UV-sterilized slide and incubated at 37°C with 5% CO2. Once the cells reached 60-80% confluency, the slides were rinsed with cell wash PBS and fixed with 4% PFA at pH 6.8 for 15 minutes. The slides were then rinsed twice with 1X PBS and dehydrated through a series of ethanol solutions: 70% ethanol for 2 minutes, 90% ethanol for 2 minutes, and 100% ethanol for 4 minutes. Slides were left to air dry at room temperature and subsequently stored at -20°C for short-term storage and at -80°C for long-term storage. Next, the slides were dehydrated again through an ascending ethanol series (70%, 90%, and 100% ethanol, each for 5 minutes at room temperature). Samples were digested in a pre-warmed digestion solution (0.01 M HCl, 0.02 mg/ml pepsin) for 10 minutes at 37°C in a water bath. The samples were then washed in 1X PBS for 5 minutes and post-fixed with 1% PFA on ice for 5 minutes. After washing in 1X PBS for 10 minutes, the slides were dehydrated through an ascending ethanol series and air-dried. Meanwhile, the DNA probe was prepared by mixing 10 μl of DNA *TERT* probe (Clone RP11-117B23, Source BioScience), which was labeled with Digoxigenin-11-dUTP (Roche, #1570013), Cot1-DNA (Life technologies, #15279-011), Herring Sperm DNA (Thermo Fisher Scientific, #15634017) and 1/20th volume ratio of 3 M sodium acetate (NaAc) with 2.5X the volume of 100% ethanol. This mixture was precipitated at -80°C for 30 minutes, centrifuged, and washed with 70% ethanol before air drying at 37°C. 10 μl of deionized formamide were added to the pellet and mixed well by shaking at 1000 rpm for 15 minutes, followed by adding 10 μl of hybridization mix per slide (20% dextran sulfate in 4X SSC pH 7.0) and shaken for at least 15 minutes before further processing. After air drying the slides, the probe was applied onto the slides, covered with a coverslip, and sealed with Fixogum. The slides were denatured on a heating block at 78°C for 10 minutes and incubated overnight in a humidified chamber at 37°C. The next day, the slides were washed with a freshly prepared Wash A solution (50% formamide in 2X SSC pH 7.0) in a water bath at 42°C with shaking for 10 minutes to remove coverslips, followed by three additional 5-minute washes. Next, the slides were washed with Wash B solution (0.5X SSC, pH 7.0, prewarmed at 60°C) at 42°C for three 5-minute washes, with gentle shaking. Blocking involved adding blocking buffer (200 μl of 4X SSC containing 3% BSA, pH 7.3) to the slide, covering them with parafilm, and incubating in a humidified chamber at 37°C for 30 minutes. For detection, 2.8 μl Anti-Digoxigenin-Rhodamine (ROCHE, #11207750910, 400 μg/ml stock concentration) in 200 μl detection buffer (blocking buffer diluted in 1:3 ratio) were added to the slides, which were then covered with parafilm and incubated in the humidified chamber at 37°C for 30 minutes, followed by incubation and washing with Wash C solution (0.1% Tween 20 in 4X SSC, pH 7.3) for three 5-minute washes at 42°C while shaking in the dark. Finally, slides were mounted using VECTASHIELD Vibrance Antifade Mounting Medium with DAPI (Vector Laboratories, #H-1800). Cell imaging and quantifications were performed using Zeiss AXIO imager 2 and ZEN 2.3 Microscopy Software for data acquisition, while ZEN 3.0 Microscopy Software and ImageJ 1.54f were used for image processing. 100 cells from each passage were quantified. GraphPad Prism 8 software was used to create graphs, perform statistical tests, and calculate *p* values. Statistical significance was assessed using a nonparametric Kruskal-Wallis test, followed by Dunn's multiple comparisons test; *p* values less below 0.05 were considered statistically significant (*$p < 0.05$, **$p < 0.01$, ***$p < 0.001$, ****$p < 0.0001$).

ALT FISH

The ALT-FISH protocol was implemented as previously described,[78] with slight modifications outlined below. A total of 50,000 cells in supplemented MEM were seeded onto UV-sterilized slides and incubated at 37°C with 5% CO2 until they reached around 80% confluency, which took between one and seven days depending on the passage number. Later, slides were washed twice with PBS, followed by fixation with 70% ice-cold ethanol for 20 minutes at room temperature. Next, the slides were washed twice with a washing buffer (100 mM Tris–HCl pH 8, 150 mM NaCl, 0.05% Tween-20), and excess buffer was carefully removed. A hybridization mix containing 2X SSC buffer, 8% deionized formamide, and 5 nM fluorescent DNA probe (5′-Atto594-(CCCTAA)5-3′, TelC probe; Eurofins Genomics) was added to the slides, which were incubated for 20 minutes at 37°C. Following hybridization, the slides were rinsed twice in 2X SSC for 5 minutes in dark cuvettes. Afterwards, slides were rinsed in ddH2O, followed by 2 minutes incubation in 70% ethanol then for 2 minutes in 100% ethanol in the dark. After the slides were air-dried, they were mounted using VECTASHIELD Vibrance Antifade Mounting Medium with DAPI. Quantification was performed on 100 cells per patient and per biological replicate across two independent replicates using a Zeiss AXIO Imager 2 microscope and ZEN 2.3 Microscopy Software. Representative images were captured using a Leica SP8 confocal microscope. Maximum intensity projections were applied using LAS X software, and further image processing was performed with both LAS X software and ImageJ 1.54f. GraphPad Prism 8 software was used to create graphs, perform statistical tests, and calculate *p* values. All values from both biological replicates are shown in the violin plot (Figure 3D). Statistical significance was assessed using a nonparametric Kruskal-Wallis test, followed by Dunn's multiple comparisons test; *p* values less below 0.05 were considered statistically significant ($N = 2$, *$p < 0.05$, **$p < 0.01$, ***$p < 0.001$, ****$p < 0.0001$).

Quantification of ecDNAs and ploidy assessment

Metaphase spreads were prepared by adding 0.04 μg/ml colcemid to dividing cells (~60% confluent) and cells were incubated for 8 hours at 37°C. Next, the supernatant was collected in a 15 ml Falcon tube, centrifuged and resuspended in 500 μl. 10-15 ml of a hypotonic solution (KCL 0.4% – prewarmed in a water bath) was added in a dropwise manner while gently mixing and incubated for 25 minutes at 37°C. After centrifugation, supernatant was removed, leaving 2-3 ml to resuspend the cell pellet. Cells were then fixated by adding 7-8 ml of ice-cold fixative solution (Methanol 3:1 glacial acetic acid) in a dropwise manner while gently mixing, followed by centrifugation and discarding the supernatant. Fixation steps were repeated twice. After discarding the supernatant, cells were re-suspended in 200-500 μl of the fixative solution, depending on the size of the pellet. For slide preparation, 20 μl of the cell suspension were dropped onto humidified pre-cleaned slides and allowed to air-dry. Slides were stored at -20°C for short-term storage and at -80°C for long-term storage. VECTASHIELD Vibrance Antifade Mounting Medium with DAPI was used for mounting the slides. Ploidy and ecDNA quantifications were performed using Zeiss AXIO imager 2 and ZEN 2.3 Microscopy Software. For ploidy counts, images were captured and analyzed using graphic tools on ZEN 2.3 Microscopy Software to identify the number of chromosomes per cell. 50 metaphases were quantified for ecDNAs and ploidy. GraphPad Prism 8 software was used to create graphs for ecDNAs, while Microsoft Excel was used to create ploidy graphs. Representative images of ecDNAs were acquired using Leica SP8 confocal microscope and data acquisition was performed using LAS X software. ImageJ 1.54f was used for further image processing.

Molecular combing for replication dynamic analysis

Newly synthesized DNA from asynchronized cells were labeled with thymidine analog 5-iodo-2'-deoxyuridine (IdU; sigma) followed by thymidine analog 5-chloro-2deoxyurdine (CldU; Sigma) both at 100 μM diluted in medium and incubated for 30 minutes, between the analogs cells were wished three times with warm PBS. After the labelling, cells were harvested and genomic DNA extracted using Fiber-Prep kit (EXTR-001, Genomic vision), combed using the Fiber-Comb, and analyzed as previously described.[79] Fluorescence detection of the IdU and CldU analogies was done by using mouse anti-BrdU (Becton Dickinson) and rat anti-CldU (Novus Biologicals) primary antibodies followed by goat anti-mouse Alexa Fluor 488 (Invitrogen) and goat anti-rat Alexa Fluor 594 (Invitrogen) for secondary antibodies, respectively. The primary antibody for fluorescence detection of ssDNA was mouse anti-ssDNA (Millipore). The secondary antibody was donkey anti-mouse Alexa Fluor 647 (Invitrogen). The length of the replication signals and the distances between origins were measured in micrometers and converted to kilobases according to a constant and sequence-independent stretching factor (1mM = 2 Kb), as previously reported.[39]

Telomere length analysis using TeloSizer

Asynchronized cells from LFS041 early, crisis and late passages and from crisis passage treated with long-term nucleosides were washed once by PBS and harvested and embedded into agarose plug (50,000/plug) using Fiber-Prep kit (EXTR-001, Genomic vision), according to the manufacturer's instructions. Two plugs from each condition were prepared, one used for quality check of the combed DNA using YOYO intercalating dye, and the other plugs were shipped at 4°C to Genomic Vision for telomere length using the TeloSizer® assay (Genomic Vision, France). Briefly, Genomic Vision melted the DNA plugs and then combed the DNA on silanized glass slides according to the EasyComb procedure (Genomic vision), the slides were then hybridized with a telomere-specific probe G-rich PNA probe Cy3-$(TTAGGG)_3$ followed by genomic DNA staining using YOYO. Telomeres at the end of chromosomes were then scanned using a FiberVision (Genomic vision) and automatically detected and measured using the FiberStudio® Easyscan software.

EU and EdU incorporation assays

For the EU assay, cells were incubated with 1mM of EU for 1 hour. Fixed with 3.7% PFA for 15 min, permeabilized with 0.5% Triton X-100 for 15 min and Click-iT reaction was performed according to the manufacturer's instructions (Click-iT RNA Alexa Fluor 594/488 Imaging Kit, Invitrogen). For the EdU assay, cells were incubated with 1mM of EdU for 1 hour. Then, cells were fixed in 3.7% formaldehyde/PBS for 15 min, washed twice with 3% Bovine serum albumin (BSA)/PBS, permeabilized with 0.5% Triton/PBS for 20 min, washed twice with 3% BSA/PBS, incubated for 30 min in EdU detection cocktail (Click-iT EDU from ThermoFisher). For further determination of DNA damage markers, the cells were proceeded to blocking solution in 3% BSA/PBS for 1hr and then processed as Immunofluorescence staining protocol. Images were analyzed using Fiji.

For the analysis of EU and damage, cells were divided into terciles based on the 33rd and 67th percentile of total EU intensity.

RNA content analysis using Acridine orange

Cells were analyzed for RNA content as previously descriped.[80] Briefly, asynchronized cells were washed in PBS and harvested, and then fixed in 70% ethanol, centrifuged and resuspended in PBS with 2mM MgCl2 (1.0 × 106 cells/ml). To assess the contribution of RNA, the cell solution was incubated with RNaseA (1000 units per 1ml, R6513, Sigma) or with DNase I (1mg/ml, Sigma) for 30 minutes at 37˚C, prior to staining with Acridine orange. Then the cell solution incubated in 66% of cold solution A (1% Triton X-100, 8mMHCl, 150mM NaCl in DDW, pH 1.2) for 45 seconds. Next, it was incubated in 66% of 10 mM Acridine orange (A6014, Sigma, diluted in 1mM EDTA, 75 mL of 150mM NaC1, 126mM Na2HPO, 37mM citric acid in DDW, pH 6) and analyzed immediately by flow cytometry (BD FACSAria III). The level of RNA is quantified by the delta between acridine orange staining intensity before and after RNase A or by comparing acridine orange staining intensity between DNase I treated conditions.

Real-time PCR

Total RNA was extracted using the Rneasy mini kit extraction kit (QIAGEN). Complementary DNA (cDNA) synthesis was performed using the High Capacity cDNA Reverse Transcription kit (Applied Biosystems). For detecting p53β, PCR was performed using specific primers (Fwd: TGGAAACTACTTCCTGAAAACAACG, Rev: AAGCTGGTCTGGTCCTGAAG) using Platinum SuperFi II Green mix (12369010, Invitrogen) and PCR products were purified using NucleoSpin kit (740609.50, MACHEREY-NAGEL) and analyzed using 2% agarose gel. For real-time PCR, RNA-free and reverse-transcriptase free reactions were used as controls. Real-time PCR was subsequently performed in ABI 7500 using a Power SYBR green PCR master Mix (Applied Biosystems). The expression level was normalized to the transcript levels of GAPDH. Specific primers used in this study are: p53 (Fwd: CAGCACATGACGGAGGTTGT, Rev: TCATCCAAATACTCCACACGC), P21 (Fwd: GGAAGACCATGTGGACCTGT, Rev: GGCGTTTGGAGTGGTAGAAA), RRM2B (Fwd: GGACAGCAGAAGAGGTCGACTTA, Rev: AAGCTTGTTCCAGTGAGGGAGA), GAPDH (Fwd: CTGTTGCTGTAGCCAAATTC GT, Rev: ACCCACTCCTCCACCTTTGA), PSAT1 (Fwd: ACTTCCTGTCCAAGCCAGTGGA, Rev: CTGCACCTTGTATTCCAGGACC). The primers used for amplification of Ribonucleotide Reductase M2 (RRM2), c-*MYC*, adenylosuccinate lyase (ADSL), IMP (inosine monophosphate) dehydrogenase1 (IMPDH1), dihydroorotate dehydrogenase (DHODH) are as described previously.[81]

Metabolomic analysis of fibroblasts from LFS patients

LFS cells from early passage (p.19–p.20), as well as from healthy skin-derived fibroblasts from non-affected individuals (LFS8 and LFS9; p.14–p.15) were used. To preserve metabolite integrity and ensure measurement accuracy, plates were briefly rinsed with ddH_2O and immediately frozen with liquid nitrogen. Samples were stored at -80°C until further processing. All conditions were prepared in five biological replicates. To ensure comparable cell numbers (~800,000–1,000,000 cells per sample), sister plates were counted, with an average of two plates per biological replicate.

Frozen plates were processed following an adjusted protocol targeting energy carriers such as NAD/NADH and NADP/NADPH.[82] This method was extended by including polarity switching and additional metabolites of interest. Briefly, cells were scratched and extracted on ice using 250 µl cooled extraction buffer (Acetonitrile : MeOH: 15 mM ammonium acetate in H2O (3:1:1), pH 10). Subsequently, samples were sonicated to ensure complete disruption of all cells using a sonication bath (Transsonic 460, Elma) for 5 min at the highest frequency on ice. Afterwards, samples were centrifuged for 15 min at 4 °C and 13,000g, and the resulting supernatant was transferred to a new LC-MS grade autosampler vial and immediately frozen at -80°C.

For metabolite separation and detection, an ACQUITY I-class PLUS UPLC system (Waters) coupled to a QTRAP 6500+ (AB SCIEX) mass spectrometer with electrospray ionization (ESI) source was used. In detail, metabolites were separated on an ACQUITY Premier BEH Amide Vanguard Fit column (100 mm × 2.1 mm, 1.7 µm, Waters) with constant column temperature of 35 °C. Separation of NAD/NADH, NADP/NADPH and additional energy carriers was achieved by the following LC gradient scheme using mobile phase A (5 mM ammonium acetate in H2O + 0.05% (v/v) ammonium hydroxide, pH 10) and mobile phase B (Acetonitrile + 0.05% (v/v) ammonium hydroxide, pH 10). An overview of multiple-reaction monitoring transitions, retention times, and MS parameters can be found in the Tables S4 and S5. Data acquisition was performed using Analyst 1.7.2 (AB SCIEX) and processed using the OS software suite 2.0.0 (AB SCIEX).

Samples were normalized based on the cell number and results from LFS8 and LFS9 were merged. Next, log fold changes (log FC) for the mean levels of detected nucleotide metabolites in LFS041 early-passage cells compared to the mean levels in non-LFS cells were calculated. Samples were excluded from the analysis in case of no value (signal to noise (S/N) < 10 or not detected). p value for each comparison calculated using one-sided t-test (*p < 0.05, **p < 0.01, value < 0.1 is indicated).

Metabolomic analysis of BJ-*hTERT* cells

Sample Preparation and extraction

Asynchronized cells were washed twice with cold (4°C) PBS, and cell metabolites immediately extracted by adding 450 µl of ice-cold (-20 °C) methanol:acetonitrile:water (v/v, 5:3:2) per 25ml plate. The lysate was collected and shaken for 10 minutes. Next, the lysate was centrifuged at maximum speed for 20 minutes at 4°C. The resulting supernatant was carefully collected and transferred to HPLC vials for analysis. Quality control (QC) samples were prepared by pooling equal aliquots from each sample group. Additionally, for MS/MS analysis, each group was pooled to create an "ID sample" to facilitate metabolite identification

LCMS data acquisition

LCMS metabolomics analysis was performed as described previously.[83] Briefly, Dionex Ultimate 300 high-performance liquid chromatography (UPLC) system coupled to an Orbitrap Q-Exactive plus Mass spectrometer (Thermo Fisher Scientific) with a resolution of 70,000 at 200 mass/charge ratio (m/z), electrospray ionization in the HESI source, and polarity switching mode to enable both positive and negative ions across a mass range of 70 to 1000 m/z, was used. The UPLC setup included a ZIC-pHILIC column (SeQuant; 150 mm × 2.1 mm, 5 µm; Merck) with a Sure-Guard filter (SS frit 0.5 µm). Five µL of the tissue extracts were injected and the compounds were separated with a mobile phase gradient of 15 min, starting at 20% aqueous (20 mM ammonium carbonate adjusted to pH 9.2 with 0.1% of 25% ammonium hydroxide) and 80% organic (acetonitrile) and terminated with 20% acetonitrile. The flow rate and column temperature were maintained at 0.2 mL/min and 45°C, respectively, for a total run time of 26 min. All metabolites were detected using mass accuracy below 5 ppm. Thermo Xcalibur was used for the data acquisition. Data processing and analysis were performed using Compound Discoverer 3.3.2.31 with an in-house library. A total of 194 metabolites were identified based on retention time (RT) and MS2 comparisons. All statistical analyses were performed using appropriate bioinformatics tools and statistical

software. Untargeted metabolomics data was processed and analyzed using MetaboAnalyst 6.0. Pathway enrichment generated in MetaboAnalyst 6.0, applying a two-sample t-test for statistical comparisons, consistent with the software's differential analysis module. Pathway impact analysis was conducted using MetaboAnalyst 6.0, with pathway significance assessed using p value threshold of < 0.05, and pathway impact scores determined based on metabolite topological analysis within each pathway.

Proteomic analysis of BJ-*hTERT* cells

Quantitative analysis was performed with Stable Isotope Labeling with Amino Acids in Cell Culture (SILAC) labeled cells as an internal standard.[84] Labeling was performed by culturing BJ-*hTERT* cells in SILAC-DMEM (DMEM without the natural lysine and arginine) and supplemented with $^{13}C_6$ $15N_2$-lysine, $^{13}C_6{}^{15}N_4$-arginine (Cambridge Isotope Laboratories) and with dialyzed FBS and antibiotics. Cells were cultured for more than 10 doublings in the SILAC medium to achieve full labeling, and the labeling incorporation was tested in a separate LC MS/MS analysis. Super-SILAC mix lysate[85] consisted of equal amounts of labeled Shp53 and Scr was combined with non-labeled BJ-*hTERT* lysate in a 1:1 ratio as a reference for quantification.

Cultured cells were lysed in a buffer including 4% SDS, 100 mM Tris HCl pH 7.6 and 100 mM DTT. Lysates were incubated for 10 min at 95 ℃ followed by short sonication. Each cell line (Shp53 or Scr) was analyzed in three biological replicates and each biological replicate was processed in two different methods. One method included protein digestion using the FASP protocol,[86] followed by fractionation to 6 fractions using strong anion exchange (SAX) chromatography.[87] The second method included methanol:chloroform protein precipitation, solubilization of the proteins with 6 M urea, 2 M thiourea in 50 mM ammonium bicarbonate, in-solution digestion, followed by strong cation exchange (SCX) fractionation into 6 fractions. Finally, all peptide samples were purified on C18 stageTip.[88] The results of the two methods for each biological replicate were averaged and analyzed as a single repeat.

LC-MS/MS analysis was performed on the EASY-nLC1000 UHPLC coupled to the Q-Exactive or QExactive Plus mass spectrometers (Thermo Scientific)[89] using EASY-Spray ionization source. Peptides were separated on a 50 cm EASY-spray PepMap column (Thermo Scientific) using a 220 min gradient of water:acetonitrile. MS analysis was performed in a data-dependent mode using a top-10 method. MS spectra were acquired at 70,000 resolution, m/z range of 300-1700 Th, a 21 target value of 3E+06 ions and a maximal injection time of 20 ms. MS/MS spectra were acquired at 17,500 resolution, a target value of 1E+05 ions, and maximal injection time of 100 ms. Raw MS files were analyzed with MaxQuant (Cox and Mann, 2008) version 1.5.0.6 and the Andromeda search engine[90] integrated into the same version. MS/MS spectra were searched against the UniprotKB database. Database results were filtered to have a maximal FDR of 0.01 on both the peptide and the protein levels. Proteomic results were analyzed based on the normalized SILAC ratio light to heavy (L/H) after normalization by subtraction of the most frequent value in each sample. Statistical tests and calculations were done using the Perseus program. Median of technical repeats were calculated prior to analysis. Data were filtered to retain only proteins with numerical values in at least 2 of 3 biological repeats of either group (Shp53 or Scr). For the comparison Welch's t-test was performed with the same parameters of permutation-based FDR=0.05 and S0=0.15.[91] Functional enrichment analysis of significantly DE proteins (Log2 fold change >1 and < -1, p value < 0.05) was performed against the human genome (Ensembl Genomes 58) by g:Profiler using a cumulative hypergeometric test. The g:SCS method was used for computing multiple testing with p value < 0.05 (http://biit.cs.ut.ee/gprofiler). Protein-protein interaction networks of significantly DE proteins were identified by the Cytoscape stringAP plugin (version 2.2.0) using a confidence score of 0.7. Networks were annotated with AutoAnnotate (version 1.5.2) and visualized in Cytoscape (version 3.10.3). Overlaps were adjusted using the yFiles Layout Algorithms (version 1.1.4).

Bulk RNA-sequencing and quantification of gene fusions

Cell pellets from two LFS patients [LFS041 p.19 (early), LFS041 p.29 (crisis), LFS041 p.65 (post-crisis), LFS041 p.346 (late), LFS087 p.20 (early), LFS087 p.47 (post-crisis) and LFS087 p.195 (late)] were prepared after trypsinization in 0.25% trypsin, cell resuspension and centrifugation. The cell pellets were kept at -80°C until performing RNA extraction using AllPrep DNA/RNA/Protein Mini Kit (QIAGEN, Cat. No.: 80004), following the manufacturer's instructions. RNA concentration was measured using NanoDrop, while a Bioanalyzer (Agilent RNA 6000 Pico Kit, Cat. No. 5067-1513) was used to measure the quality of the RNA. Sequencing libraries were prepared with the Illumina TruSeq mRNA stranded Kit following the manufacturer's instructions. Briefly, mRNA was purified from 500 ng of total RNA using oligo(dT) beads. Poly(A)+ RNA was fragmented to 150 bp and converted to cDNA. The cDNA fragments were then end-repaired, adenylated on the 3′ end, adapter ligated and amplified (15 cycles of PCR). The final libraries were validated using the Qubit® RNA BR Assay Kit (Thermo Fisher Scientific, Cat.No. Q10211) and the TapeStation RNA ScreenTape assay (Agilent Technologies, Cat. No. 5067-5576, 5067-5577). 2x 100 bp paired-end sequencing was performed on the Illumina HiSeq 4000 following the manufacturer's protocol. All passages from one given patient-derived culture were processed and sequenced together.

Data Processing and Alignment

DKFZ/ODCF RNAseq workflow (version 1.3.0) was used to analyze RNA sequencing data.[92] The specific versions of the components used include the alignment and quality control workflows (version 1.2.73-3),[93] Roddy default plugin (version 1.2.2),[94] Roddy base plugin (version 1.2.1),[95] and Roddy (version 3.5.9).[96]

In brief, a two-pass alignment approach with the STAR aligner was used to align FASTQ reads for individual samples (version 2.7.10a).[97] The alignment was performed to a STAR index created from the 1000 Genomes assembly and gencode version 19

gene models, utilizing sjdbOverhang of 200. Duplicate reads in the main alignment file were marked using Sambamba (version 0.6.5).[98] Samtools was used to sort the Chimeric file (version 1.6),[99] followed by duplicate marking and generating of BAM files with Sambamba. Quality control was carried out using the Samtools flagstat command and the RNA-SeQC tool (version 1.1.8).[100] Gene-specific read counting over exon features was conducted using Subreads (version 1.6.5),[101] based on the Gencode v19 models. A custom script was used to compute RPKM and TPM expression values. Gene fusion detection was performed using Arriba.[102] We focused on the high-confidence fusion events.

Differential gene expression analysis

Differential gene expression analysis was performed using the NOISeq package (version 2.46.0)[103,104] within R studio (version 4.3.0.) (https://rstudio.com), in order to compare between passages within individual patients. We used the following key parameters: no normalization (norm = 'n'), a probability threshold for non-replicability (pnr = 0.2), a noise threshold (v = 0.02), and a minimum expression level (lc = 1), to ensure robust detection of significant expression changes.

Gene set enrichment analysis (GSEA) of gene ontology (GO) was performed using the clusterProfiler package (version 4.8.3)[105] in R studio, with gene annotations supported by org.Hs.eg.db (version 3.18.0).[106] Pathways were considered significant if they had an adjusted *p* value (FDR) below 0.05, determined by the Kolmogorov–Smirnov test with Benjamini-Hochberg correction. Plots of GSEA results were created using ggplot2 (version 3.5.1)[107] for visualizing enriched pathways. Heatmaps illustrating expression patterns were generated using pheatmap package (version 1.0.12)[108] in R studio, by selecting gene sets based on specific biological processes identified in GSEA-GO results or those hypothesized to play a pivotal role in the mechanism, even if not significantly enriched in GSEA. RNA expression data were visualized by clustering genes and samples based on their expression patterns using hierarchical clustering with Euclidean distance.

Sanger sequencing of *TP53* mutation sites in LFS

Genomic DNA was extracted from LFS cells using GenElute (G1N70-1KT, Sigma). The mutation site of the *TP53* gene was amplified by PCR with specific primers (Fwd: TACTCCCCTGCCCTCAACAA, Rev: ACAAACACGCACCTCAAAGC) using Platinum SuperFi II Green mix (12369010, Invitrogen). PCR products were purified using the NucleoSpin kit (740609.50, MACHEREY-NAGEL). Sanger sequencing was performed using inner PCR primers (Fwd: TGTGCAGCTGTGGGTTGATT, Rev: TGTTCCGTCCCAGTAGATTACC) at Hylab or Genomic Technologies Facility, Hebrew university Jerusalem. Sequencing data were analyzed using FinchTV.

Bulk whole-genome sequencing

Cell pellets from LFS fibroblasts (LFS041 p.63, post-crisis and LFS087 p.195, late) were prepared after trypsinization in 0.25% trypsin, cell resuspension and centrifugation. Cell pellets were kept at -80°C until performing DNA extraction using DNeasy Blood & Tissue Kit (QIAGEN; Cat. No.: 69504), following manufacturer's instructions. stranded DNA assay Qubit dsDNA HS Assay Kit-100 assays (Life Technologies Q32851) was used to quantify the DNA, while a Bioanalyzer (Agilent High Sensitivity DNA 5067-4626) was used to measure the quality of the DNA. Sequencing libraries were prepared using the Illumina TruSeq HT Library Prep Kit following the manufacturer's instructions. Briefly, 100 ng of genomic DNA was fragmented to ~350 bp using a Covaris ultrasonicator (Covaris, Inc.). The fragmented DNA was then end-repaired, size-selected using magnetic beads, extended with an 'A' base on the 3′ end and ligated with TruSeq paired-end indexing adapters. The adapter-ligated fragment libraries were enriched using 8 cycles of PCR and purified 1-2 times using magnetic beads. The generated libraries were validated using the Qubit® dsDNA BR Assay Kit (Thermo Fisher Scientific, Cat.No. Q32853) and using the TapeStation Genomic DNA ScreenTape assay (Agilent Technologies, Cat. No. 5067-5365, 5067-5366). Whole genome sequencing was done using the Illumina NovaSeq 6K paired-end 150 SP platform.

Analysis of bulk whole-genome sequencing data

Whole-genome sequencing data were processed by the DKFZ OTP pipeline.[109,110] Briefly, reads were aligned to the 1000 Genome project version of the GRCh37 (hg19) reference genome[111] using BWA-MEM (version 0.7.15).[112] Duplicates were marked with Picard (version 2.25.1)[113] and later removed with SAMtools[114] together with low quality reads. The resultant BAM files were used as input to the analyses described below.

OncoAnalyser

Bulk WGS derived BAM files were then run through the nf-core OncoAnalyzer nextflow pipeline (v0.5.0)[115] based on tools developed by the Hartwig Medical Foundation, running in tumor-only mode. In brief, this pipeline calls SNVs using the HMF developed mutation-caller SAGE,[116] structural variants using GRIDSS,[117] haplotype resolved copy number variation using PURPLE,[118] and then clusters and annotates structural variant clusters using LINX.[118]

AmpliconSuite

AmpliconSuite[119] (v1.2.2) was run on the BAM files generated by the DKFZ OTP (described above) to identify putative highly amplified extra-chromosomal DNA fragments. CNVkit[120] (v0.9.10) was first used to segment read counts across the genome and detect copy number changes using the circular binary segmentation algorithm.[121] Copy number altered segments with copy state of at least 4.5 and minimum length of 50 kb were then used as seeds to AmpliconArchitect[122] to reconstruct the structures of these focally amplified regions, followed by AmpliconClassifier to obtain a list of possible circular and ecDNA structures and BFB cycles.

CellPress
OPEN ACCESS

Chromothripsis detection

To identify chromothriptic chromosomes, CNV calls from OncoAnalyser were first filtered for events larger than 500 bases and then used as input for the ShatterSeek R package (version 1.1)[28] together with the corresponding somatic SVs. This method first identifies the largest SV event cluster by forming an SV-graph where individual events are connected when their breakpoints are interleaved, and then selecting the largest connected component per chromosome. The distributions of SV breakpoints and end-joining orientations are then tested against a series of criteria, looking for evidence for or against the random distribution expected in a chromothripsis event. The number of CNV events overlapping the regions affected by this SV cluster is also calculated, and this information is combined to determine a label for chromothripsis in each chromosome, as described in more detail in Cortés-Ciriano et al.[28] For our application of this method, we used a CNV cutoff of 7 oscillating events (between 2 or 3 states), and an FDR of 0.2 for determining statistical significance. The oncoanalyser SVs and CNVs, together with the statistical criteria calculated by ShatterSeek were then visualized using the ReConPlot R package (version 0.2).[123]

Single-cell DNA sequencing by HIPSD-seq and HIPSD&R-seq

Tn5 loading

A high-activity Tn5 transposase[124] was used instead of the Tn5 transposase provided in the 10X Multiome kit. Annealing buffer (50 mM NaCl, 40 mM Tris, pH 8) was utilized to resuspend lyophilized adapter oligonucleotides at a concentration of 100 μM. The adapters were pre-annealed on a thermocycler by heating at 85°C for 2 minutes, followed by a gradual cooling to 20°C at a rate of 1°C per minute. For HIPSD-seq,[29] Read1 (5′-TCGTCGGCAGCGTCAGATGTGTATAAGAGACAG) was annealed with blocked-phos-ME (5′-[Phos]C*T*G*T*C*T*C*T*T*A*T*A*C*A*[23ddC]), while Read2 (5′-GTCTCGTGGGCTCGGAGATGTGTATAAGAGACAG) was annealed with blocked-phos-ME. For HIPSD&R-seq,[29] phos-Read1 (5′-[Phos]TCGTCGGCAGCGTCAGATGTGTATAAGAGACAG) was annealed with phos-ME (5′-[Phos]C*T*G*T*C*T*C*T*T*A*T*A*C*A*C*A*T*C*T) – phos: 5′ phosphorylation, *: PTO modification, and phos-Read2 (5′-[phos]GTCTCGTGGGCTCGGAGATGTGTATAAGAGACAG) with phos-ME. Adapters were mixed with an equal volume of 100% glycerol and stored at -20°C. Tn5 assembly involved mixing the transposase with the annealed primers in equal volumes, followed by incubation at room temperature for 30 minutes. The assembled Tn5 was subsequently diluted to a final concentration of 83 μg/ml in dilution buffer (50 mM Tris pH 7.5, 100 mM NaCl, 0.1 mM EDTA, 1 mM DTT, 0.1% NP-40, 50% glycerol) for HIPSD-seq.[29]

Sample preparation

For HIPSD-seq, cells from LFS041 p.27 (crisis) and LFS041 p.62 (post-crisis) were harvested after trypsinizing the cells with 0.25% trypsin and resuspending them in PBS. For HIPSD&R-seq, cells from LFS041 p.22 (early) and LFS087 p.196 (late) were harvested in the same way, and resuspended in PBS with 1% BSA.

Nuclei extraction and nucleosome depletion

For HIPSD-seq, fixation was performed by incubating 1 × 10^6 cells in 1 ml of 1.5% methanol-free formaldehyde (FA; Thermo Fisher Scientific, #28906) in PBS for 10 minutes at room temperature while gently shaking. 200 mM glycine was added for fixation neutralization, followed by ice incubation for 5 minutes. The cells were then centrifuged at 550 g for 5 minutes at 4°C and washed with ice-cold PBS. To isolate nuclei, the cells were resuspended in 1 ml of ice-cold NIB buffer (10 mM Tris-HCl; pH 7.4, 10 mM NaCl, 3 mM MgCl2, 0.1% Igepal and 1X protease inhibitor cocktail, #5871S, Cell Signaling Technology), followed by incubation on ice with gentle mixing for 20 minutes. The nuclei were centrifuged at 500 g for 5 minutes at 4°C and washed once with 1X NEBuffer 2.1 (NEB, #B7202). For the nucleosome depletion step, nuclei were resuspended in 1X NEBuffer 2.1 containing 0.3% SDS (Serva, #20767), followed by incubation at 42°C for 15 minutes with shaking. The SDS was quenched by adding 2% Triton X-100 (Sigma-Aldrich, #93443) and incubating at 42°C with shaking for 15 minutes. The nuclei were then centrifuged at 500 g for 5 minutes at 4°C and resuspended in 1X Nuclei Buffer (10X Genomics). Luna-FL™ cell counter (Logos Biosystems) was used to count the nuclei, which were then diluted to a final concentration of 2000–5000 nuclei/μl.

For HIPSD&R-seq, the protocols for fixation with 1.5% FA, nuclei isolation with NIB buffer, and nucleosome depletion using 0.3% SDS were carried out as described above for HIPSD-seq. However, all buffers used during and after nuclei isolation (i.e. to NIB buffer and 1X NEBuffer 2.1) were supplemented with 1 U/μL RNAse inhibitor (Takara Bio, #2313A). After nucleosome depletion quenching with 2% Triton X-100, nuclei were centrifuged at 500 g for 5 minutes at 4°C and resuspended in 1X Nuclei Buffer (10X Genomics) containing 1 U/μl RNAse inhibitor. Finally, the nuclei were counted using a Luna-FL™ cell counter and diluted to a concentration of 2000–5000 nuclei/μl.

HIPSD-seq

1.67 x 10^6 cells from LFS041 p.27 and 1.1 x 10^6 cells from LFS041 p.62 were used for nuclei isolation and nucleosome depletion as described earlier. The nucleosome-depleted nuclei were processed following the 10X ATAC protocol described in the Chromium Single Cell ATAC Reagent Kits User Guide v1.1 Chemistry (CG000209, 10X Genomics), with the modification that the provided transposase was substituted with a highly active in-house Tn5 (83 μg/ml). For transposition, 10,000 nuclei were loaded onto the Chromium Next GEM Chip H (PN-1000161). Single-cell DNA libraries were prepared using the standard reagents of the Chromium Next GEM Single Cell ATAC Library & Gel Bead Kit v1.1 (PN-1000176), with unique indexing applied via the Single Index Kit N Set A (PN-1000212). Qubit 3.0 Fluorometer (#Q33216, Invitrogen) and the 4200 Tapestation system (Agilent Technologies) were used for quality control and to perform molarity calculations of the final libraries. Sequencing of the libraries was performed on the NovaSeq 6000 platform with paired-end 100 SP reads: 51 cycles for read 1, 51 cycles for read 2, 8 cycles for i7, and 16 cycles for index 2, with 1% PhiX spike-in.

HIPSD&R-seq from fibroblasts

A total of 4.3 x 10^5 cells from LFS041 p.22, while 5 x 10^5 cells each from LFS041 p.67 and LFS087 p.196 were pooled (1:1 ratio)[29] for the mixed patient experiment for HIPSD&R-seq were used for nuclei isolation and nucleosome depletion as described above. 10X Multiome protocol, according to the Chromium Next GEM Single Cell Multiome ATAC + Gene Expression Reagent Kits User Guide (CG000338, 10X Genomics) was used to process the nucleosome-depleted nuclei. For transposition, 10,000 nuclei were loaded onto the Chromium Next GEM Chip J (PN-1000230), with the 10X Genomics transposase replaced by a highly active in-house Tn5. Both scDNA and scRNA libraries were prepared using the standard reagents provided in the Chromium Next GEM Single Cell Multiome ATAC + Gene Expression Reagent Bundle (PN-1000285). The scDNA libraries were indexed with the Single Index Kit N Set A (PN-1000212), whereas the scRNA libraries were indexed with the Dual Index Kit TT Set A (PN-1000215). Qubit 3.0 Fluorometer (#Q33216, Invitrogen) and the 4200 Tapestation system (Agilent Technologies) were used for quality control and to perform molarity calculations of the final libraries. Sequencing of scDNA libraries was performed on the NovaSeq 6000 platform (200 cycles, S4) with 101 cycles for read 1, 101 cycles for read 2, 8 cycles for i7, and 24 cycles for i5. scRNA libraries were sequenced using the NovaSeq 6000 platform (paired-end 100 SP), with 28 cycles for read 1, 90 cycles for read 2, and 10 cycles each for i7 and i5. All libraries were sequenced using 1% PhiX.

Computational analysis

The initial preprocessing of HIPSD-seq (crisis and late passage) and HIPSD&R-seq (early passage and the mixed experiment) data was performed with Cell Ranger ATAC pipeline (version 2.1.0), with a reference provided by 10x Genomics (Cell Ranger Arc, GRCh38, version 2020-A). In the case of HIPSD&R-seq, only the DNA component was analysed. Because the default cell definition from Cell Ranger is not appropriate for samples with depleted nucleosomes, the cells were defined based on the barcode rank plot (log(fragments) vs log(rank)). Only cells above the highest gradient were used for further processing.

The initial BAM output from Cell Ranger was then split into single-cell BAM files with a command 'bamsplice' from Cell Ranger DNA pipeline (version 1.1.0). Next, single-cell BAM files were filtered to retain only high-quality reads with SAMtools.[114] To extract the number of counts per 1MB bin size, hmmcopy_utils was used.[125] Only cells with more than 90% of non-empty bins and 60,000 counts were kept for copy number calling with HMMcopy (version 1.42.0).[126] When running HMMcopy, the e value was set to 0.9999. Because we previously observed a tendency of HMMcopy to overcall homozygous deletions in our data, we encoded both, homozygous and heterozygous deletions as a loss with 0-1. Finally, CNAs were plotted with ComplexHeatmap,[127] only using genomic bins that are annotated as ideal by HMMcopy.

For the mixed-patient (LFS041 p.67: LFS087 p.196 = 1:1) HIPSD-seq experiment, the data was processed as described above. However, the next approach was used to select only the cells from the patient LFS087 p.196. Single-cell CNA profiles of all the cells were correlated (Pearson's correlation) to bulk CNA profiles for both patients. In order for a cell to be classified as LFS087 p.196, the cell needed to have higher correlation to the bulk CNA profile of the patient LFS087 than to the CNA profile of the patient LFS041.

Strand-seq analysis

Strand-seq libraries were prepared following the protocol detailed previously[26] with minor modifications. The key steps of the procedure are summarized below. In brief, BrdU incorporation was carried out using growing cells from three distinct passages from LFS041 (p.22 (early), p.63 (post-crisis) and p.343 (late)). Cells were labeled with 40 μM BrdU (Sigma, B5002) for a single round of cell division. This step is crucial as cells with incomplete BrdU incorporation or those that have undergone multiple DNA synthesis phases with BrdU present will yield unreliable strand-specific sequencing data. Cells were frozen and stored at -80°C until further processing. Upon thawing in supplemented MEM medium, cells were centrifuged and resuspended in Nuclei Staining Buffer A to a final concentration of 1 x 10^6 cells/ml. The buffer composition was as follows: 100 mM Tris–HCl (pH 7.4), 154 mM NaCl, 1 mM CaCl2, 0.5 mM MgCl2, 0.2% BSA, 0.1% NP40 (Sigma-Aldrich, Cat. No. 74385), 10 μg/ml Hoechst 33258 (Enzo Life Sciences, Cat. No. ENZ-52402) in ultra-pure water. The cell suspension was filtered through a cell strainer and incubated on ice for approximately 30 min. Single cells were then sorted into individual wells of a 96-well plate using fluorescence-activated cell sorting (FACS), each containing 5 μl of TheraPEAK ProFreezeTM Freezing Medium (Lonza, Cat, No. BEBP12-769E) and the plate was stored at -80°C until further use. Following thawing, DNA MNase fragmentation was carried out by incubating the samples with 0.5 U (Unit) Micrococcal Nuclease (NEB, Cat. No. M0247S) in MNase buffer supplemented with 1.5 mM DTT (Sigma-Aldrich, Cat. No. 43816) and 5% PEG 6000 (Calbiochem, Cat. No. 528877) for 8 min at room temperature, in a total reaction volume of 15 μl/well. The enzymatic reaction was terminated by adding 10 mM EDTA. DNA purification was performed using AMPure XP beads (Beckman Coulter, Cat. No. A63881) at a 1.0X ratio, with subsequent elution in 10 μl EB Buffer, utilizing a Biomek FXp liquid handling robotic system to facilitate large-scale library preparation. End-repair was carried out by incubating the samples for 30 min at room temperature with a mixture containing 0.3 U/μl T4 DNA polymerase (NEB, Cat. No. M0203S), 0.1 U/μl Klenow DNA polymerase (NEB, Cat. No. M0210S), and 1 U/μl T4 polynucleotide kinase (NEB, Cat. No. M0201S), 1x T4 ligase buffer (NEB, Cat. No. B0202S) and 2 mM dNTP mix (NEB, cat. no. N0447S), whereas 2.5 μl of the mixture was added to each well. Following this step, the DNA again underwent clean up using AMPure XP beads at a 1.8X ratio, employing the Biomek FXP liquid handling robotic system to maintain consistency and efficiency. Next, A-tailing was performed by adding 1.5 μl of A-tailing Master Mix to each well, which contained 1.67 U/μl Klenow Fragment (3′→5′ exo−; NEB, Cat. No. M0212S) and 1.67 mM dATP (NEB, Cat. No. N0440S). The samples were incubated at 37°C for 30 min, then purified with AMPure XP beads at a 1.8X ratio. Subsequently, adapter ligation was performed by incubating DNA fragments with forked Illumina adaptors in a master mix prepared using 0.0893 μM PE adaptors (Illumina PE

adaptor-1: 5'-[Phos]GATCGGAAGAGCGGTTCAGCAGGAATGCCGAG-3′, Illumina PE adaptor-2: 5′-ACACTCTTTCCCTACAC GACGCTCTTCCGATC*T-3′ – *: phosphorothioate bond between the last two nucleotides), 2.67x T4 Quick Ligation Reaction Buffer, and 0.144 U/μl Quick Ligase (NEB, Cat. No. M2200L; with the included buffer), diluted in Ultrapure H2O to a final volume of 7.5 μl per well. After adding the master mix to the DNA fragments, the reaction volume reached 20 μl, resulting in a final adaptor concentration of 33.5 nM per cell. The ligated DNA was purified once more using AMPure XP beads at a 1.6X ratio and eluted in a volume of 9.5 μl. Subsequently, the DNA was incubated with 10 μg/ml Hoechst 33258 for 15 min, followed by UV irradiation. The irradiation was carried out using a crosslinker equipped with five 365-nm longwave UV bulbs for 15 min, delivering a total dose of 2.7 x 10^3 J/m^2. The nicked DNA was amplified using a combination of 96-well-custom multiplexing Primer PE 2.0 (5′-CAAGCAGAAGACGGC ATACGAGAT NNNNNNCGGTCTCGGCATTCCTGCTGAACCGCTCTTCCGATCT-3′), which includes a combination of oligonucleotides each containing a 6-bp (hexamer) multiplexing barcodes (Sigma-Aldrich), and Primer PE 1.0 (Illumina) (5′-AATGATACGGCGACCACCGA GATCTACACTCTTTCCCTACACGACGCTCTTCCGATCT-3′). First, 1 μl of Primer PE 2.0 was added per well, followed by 12.5 μl of Phusion HF PCR Master Mix (NEB, Cat. No. M0531L) and 1 μl of Primer PE 1.0, bringing the total reaction volume to 25 μL. Thermal cycling conditions were as follows: initial denaturation at 98°C for 30 seconds, followed by 18 cycles of denaturation at 98°C for 10 sec, annealing at 65°C for 30 sec, and extension at 72°C for 30 sec. A final extension step was carried out at 72°C for 5 min. Post-amplification, the DNA from all wells was pooled and subjected to purification and size selection using AMPure XP beads at a 0.8X ratio. This step served to remove free primers and adapter dimers. The resulting libraries were sequenced on a NextSeq500 platform using a MID-mode, 75bp paired-end protocol. Following sequencing, the data was demultiplexed, aligned to the hg38 reference assembly using BWA mem (0.7.17-r1188),[112] and duplicate reads were mapped using sambamba (v1.0).[98]

Strand-seq data processing

Strand-seq data was processed using the MosaicCatcher pipeline (v2.0.1).[26] Mapping quality filtered (MAPQ > 10) and non-duplicated reads were used to generate read-counts per 200kb bin for Watson and Crick strands separately in each cell. Read counts per bin were then visualized per chromosome and cell. Prior to downstream analysis, cells were manually filtered based on their visualized read count distributions to exclude noisy cells (those exhibiting spiky peaks, high background or uneven coverage), cells with incomplete BrdU incorporation, cells with fewer than 200,000 reads, and those displaying all-Watson or all-Crick chromosomes or extremely skewed Watson/Crick ratios (>80% Watson or >80% Crick). For the remaining cells, the read counts per strand and chromosome were segmented, haplotype-resolved using StrandPhaseR and fed into MosaiClassifier to create initial SV calls per cell.

Ideograms generated using Mosaicatcher were used to profile structural variations, including deletions, duplications, inverted duplications, inversions, and complex rearrangements, in single cells across different passages using Microsoft Excel. Each structural variant was mapped to its genomic position in megabase resolution for individual chromosomal arms after detailed examination of each cell. This comprehensive approach facilitated variant calling and enabled us to create a matrix of all possible structural variations for each cell.

Clustering of Single Cells Based on Structural Variants

Next, we took two approaches to cluster single cells based on structural variant annotations per-cell detected from StrandSeq (as described above). The first approach was event-based. For this approach, unique breakpoints detected across all cells were used to segment the genome. For each cell, the presence or absence and the type of structural variant at each segment was recorded. The second approach was bin-based. Here the genome was binned into approximately 2 MB bins, with equal bin-sizes per chromosome derived from the tile function as implemented by the GenomicRanges R package (v1.52.0).[128] For each cell and segment derived from binning, a structural variant was recorded if it was detected by Strand-seq to overlap that segment within that cell. In the case of two or more structural variants overlapping the same segment, the SV overlapping the greater number of bases within the segment was assigned. In both cases, a virtual diploid cell which is unmodified at each genomic segment was added for subsequent rooting of phylogenetic trees. For both genome segmentation approaches, distance between cells was then calculated using a modified Hamming distance, where for each pair of cells, each segment contributed a distance of 1 if the event recorded for that segment did not match, except for a comparison between unmodified and complex segments, which contributed a distance of 2. This was chosen to account for the fact that the "complex" structural variant annotation as described above can arise from the overlap of multiple simple SVs in the same genomic location. The cells were then clustered using the neighbor joining method as implemented by the ape R package (v5.7-1). For visualization purposes, the ape package was used to plot the resulting clustering as phylogenetic trees, rooted at the virtual diploid cell added to the data. Finally, main structural variance differences and shared events between main clusters were annotated manually based on the matrices created earlier using Excel.

Fold-back inversions calling (BFB patterns) in strand-seq data

We analyzed the strand-seq data to identify fold-back inversions in single cells, which are hallmark features of BFB events.[129] Fold-back inversions were quantified by searching for characteristic patterns on all chromosomal arms, defined as small amplifications involving either the H1 (haplotype 1), H2 (haplotype 2) strand or both, followed by a deletion. The classification of fold-back inversions and their connection to BFB cycles was guided by previously defined structural rearrangement footprints.[129] GraphPad Prism 8 software was used to create graphs, perform statistical tests and calculate *p* values. Fisher's exact test was performed for pairwise comparisons between each of the three passages. To account for the differences in the number of single cells detected and analyzed in each of the three passages, results were normalized accordingly, and *p* values were adjusted as comparisons were made across the three passages.

Analysis of hypertranscription in a public dataset

We re-analyzed data from a study on hypertranscription, which encompasses RNA output levels from 7494 patients from The Cancer Genome Atlas (TCGA) across 31 cancer types.[40] The authors of this study calculated the hypertranscription scores using the RNAmp method, which compares the allelic ratio of somatic mutations in RNA to their corresponding ratio in DNA, leveraging the increased representation of transcribed alleles in RNA compared to DNA. The patient IDs of the same 7494 patients were used to classify them into two groups based on their respective *TP53* and *MDM2* status from the publicly available TCGA dataset through the Genomic Data Commons (GDC) portal. The first group included tumors with WT *TP53* and *MDM2* (WT *TP53*/*MDM2*), while the second group consisted of tumors with *TP53* loss, *MDM2* gain, or both ($TP53^-/MDM2^+$/$TP53^-MDM2^+$), which are referred to as $TP53^-/MDM2^+$ in the main text. Both heterozygous and homozygous CNAs were considered. After filtering, the dataset contained 6,305 tumor samples, split into 4032 $TP53^-/MDM2^+$ and 2273 WT *TP53*/*MDM2* tumors.

The fold increase in RNA output, namely the hypertranscription fold change (hytx_fch) was used to compare the hypertranscription status between the two groups. The comparison was performed based on the total number of patients, regardless of the tumor type, as well as for each tumor type separately. For comparisons within each cancer type, a minimum sample size of 50 patients per group was required to ensure statistical robustness. Tumor types that did not meet this criterion were excluded from the analysis. A subset of selected tumor types is presented in (Figures S14D–S14K). GraphPad Prism 8 software was used to create graphs, perform statistical tests and calculate *p* values. Statistical significance was assessed using a non-parametric t-test (Mann-Whitney test) to compare two independent groups, as the data were not normally distributed. *p* values less than 0.05 were considered statistically significant ($^*p < 0.05$, $^{**}p < 0.01$, $^{***}p < 0.001$, $^{**}p < 0.0001$).

QUANTIFICATION AND STATISTICAL ANALYSIS

Statistical analyses employed tests described in the respective methods sections and specified in the figure legends or the main text as appropriate. Statistical significance was defined as a *p* value less than 0.05, and multiple testing corrections were applied when needed. Sample sizes were not predetermined using statistical methods, and all collected data were included in the analyses. Detailed information on biological replicates and experimental repetitions is provided in the respective figure legends.

Graphs, statistical analyses, and *p* value calculations were conducted using GraphPad Prism 8 or 10 software, unless otherwise stated. All values are reported as mean ± standard error of the mean (SEM) or mean ± standard deviation of the mean (SD) as indicated.